공학박사 학위논문

Modeling of the Density Pump-out by Double-null Transition in KSTAR Discharge

KSTAR 더블널 전이 실험에서의

밀도 저하 모델링

2023 년 2 월

서울대학교 대학원

에너지시스템공학부

이 재 곤

Modeling of the Density Pump-out by Double-null Transition in KSTAR Discharge

지도 교수 나 용 수

이 논문을 공학박사 학위논문으로 제출함
2023 년 2 월

서울대학교 대학원
에너지시스템공학부 원자핵공학전공
이 재 곤

이재곤의 공학박사 학위논문을 인준함
2023 년 1 월

위 원 장 황 용 석 (인)

부위원장 나 용 수 (인)

위 원 함 택 수 (인)

위 원 이 정 표 (인)

위 원 이 형 호 (인)

Abstract

Jae Gon Lee
Department of Energy Systems Engineering
The Graduate School
Seoul National University

Nuclear fusion energy, which has been noted as an environmentally friendly and sustainable energy source, has been studied for its possibility in a tokamak device that confines plasma with a magnetic field. KSTAR, a Korean tokamak device, paid attention to the advantages of the DN (Double Null) among these magnetic field configurations and experimented with the transition from the SN (Single Null). In this experiment, it was observed that the performance constantly increased as the plasma density gradually decreased during the transition process.

In this study, three reasons for the gradual decrease in density that occurred in this KSTAR DN transition discharge were presented and modeled to demonstrate their validity. First, the effect on the core plasma density through the recycling of plasma ions in the inner divertor region was compared based on the magnetic field configuration. When only the flow parallel to the magnetic field is considered, that is, when the plasma drifts are not considered, the recycling rate near the inner divertor does not have a significant effect on the core plasma density. The following reason is that the

effect of ▽B drift changes during the DN transition, inducing more convection so to lower the density. This was found through modeling to be caused by the change in the convective direction of the ▽B drift in the High Field Side (HFS) according to the difference in the magnetic field configuration. As a result of investigating the change in density by adding ▽B drift to SN (Single Null) and DN plasma, which previously converged without the drift, it was calculated that the density decreased more significantly in the DN configuration. Finally, an increase in the plasma recycling rate in the inner divertor due to E×B drift was suggested as the reason. When the direction of the magnetic field makes ▽B drift directed toward the X-point, the flow of E×B forms an inward flow from the outer diverter near the X-point. However, in the region near the opposite X-point, the direction of the flow is reversed and the particle flow is directed toward the outer divertor where the gas outlet is located. In other words, as found through the plasma modeling, in the SN configuration, a large increase in the edge pedestal density was observed due to the high recycling rate near the inner diverter. Still, in the DN configuration, this fueling effect was very small due to the effect of the opposite flow.

In addition, in this study, the modeling requirements for the plasma modeling were organized, and a two-dimensional tokamak plasma transport modeling system was established that integrates the core-edge-SOL area that satisfies these requirements. In the core plasma modeling of this study, various plasma transport phenomena are not considered (such as turbulence or MHD mode). However, since the plasma profile can be converged through the experimentally calculated plasma transport coefficients and the two-dimensional interaction with the SOL is included, it was sufficient to investigate

the response of the phenomenon occurring in the core and SOL. In addition, through plasma modeling up to the wall of the tokamak chamber through upgrading the grid generator, artificial boundary conditions could be excluded as much as possible, and the transport of reused particles could be calculated more comprehensively. Therefore, this system can perform plasma transport calculations from the walls to the core plasma to be able to model the reasons suggested above by implementing two-dimensional drifts in the system.

Keywords: Tokamak, Plasma, Plasma Modeling, Density Pump-out, Plasma Drift, Magnetic Field Configuration.

Student Number: 2017-32731

Table of Contents

List of Figures

List of Tables

Chapter 1.
Introduction

1.1. Background

1.1.1. Fusion Energy

As extreme weather events around the world become more severe and frequent each year, the need for more environmentally friendly energy sources to reduce greenhouse gas emissions is soaring. As such energy sources, renewable energy sources such as wind energy, solar energy, and geothermal energy are attracting attention, and scientific and policy attempts and support are being made in countries around the world. However, problems that are not free from variables such as weather, season, and region inevitably occur due to the nature of the renewable energy generation method. For this reason, baseload energy is vital for the national energy strategy, that's why nuclear fusion energy has been steadily developed since the discovery of nuclear energy.

Nuclear fusion is a process in which light nuclei fuse together to form heavier nuclei, as shown in Figure 1, and the reduced mass is converted into energy. In this process, the atomic nuclei must come very close together in order to receive the nuclear force and fuse, but because they are positively charged, they must overcome the electrical force. This repulsive force is called the Coulomb barrier or fusion barrier energy. It decreases as the electrical repulsive force decreases and the nuclear force increases due to the large nuclear mass. So, the following D (Deuterium)−T (Tritium) reaction is attracting the most attention.

$$D + T \rightarrow He^4\ (3.52\ MeV) + n\ (14.06\ MeV). \tag{1.1}$$

However, even in the case of this D−T reaction, since the probability of the fusion reaction is very low, a method of increasing the number of reactions is required. In order to increase this, a massive number of particles (density) or high energy (temperature) must be achieved.

In a star like Sun, the probability of collision increases by the high density due to the gravity generated by its enormous mass, and the nuclear fusion reaction actively occurs. However, since this is close to impossible on Earth, two major confinement methods have been proposed. The first is inertial confinement fusion, in which energy is applied to purified raw material (pellet) with a powerful laser, etc., and the internal raw material is compressed by an explosion generated from the outside, creating an environment of

high density and temperature to induce a nuclear fusion reaction. Recently, the National Ignition Facility (NIF) of the United States demonstrated the possibility of obtaining a nuclear fusion energy of 3.15 MJ, which is greater than the input energy (2.05 MJ) [1].

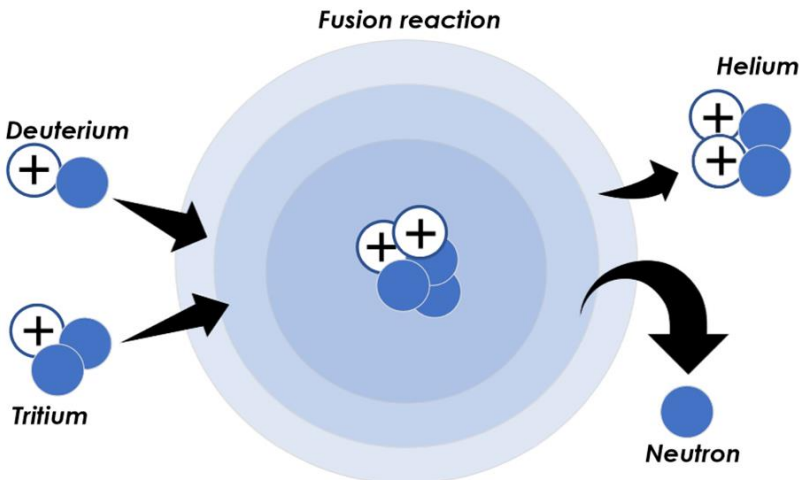

Figure 1. Cartoon of the deuterium (D) and tritium (T) nuclei collide and fuse, releasing helium and neutrons [2]

The second method is to confine and maintain ionized plasma particles through a strong magnetic field. Plasma, also called the fourth state of matter, refers to a state in which atomic nuclei and free electrons exist separately. These plasma particles are

electrically charged and respond immediately to electromagnetic fields applied from the outside. Therefore, in an ideal situation, when a strong magnetic field is applied from the outside using a donut-shaped (toroidal) solenoid, the plasma particles flow along the magnetic flux (frozen to the flux), so they cannot be reached the Plasma Facing Components (PFCs). Tokamak and Stellarator are the device concepts designed using this principle. The difference between the two is whether or not a magnetic field is induced by the internal plasma.

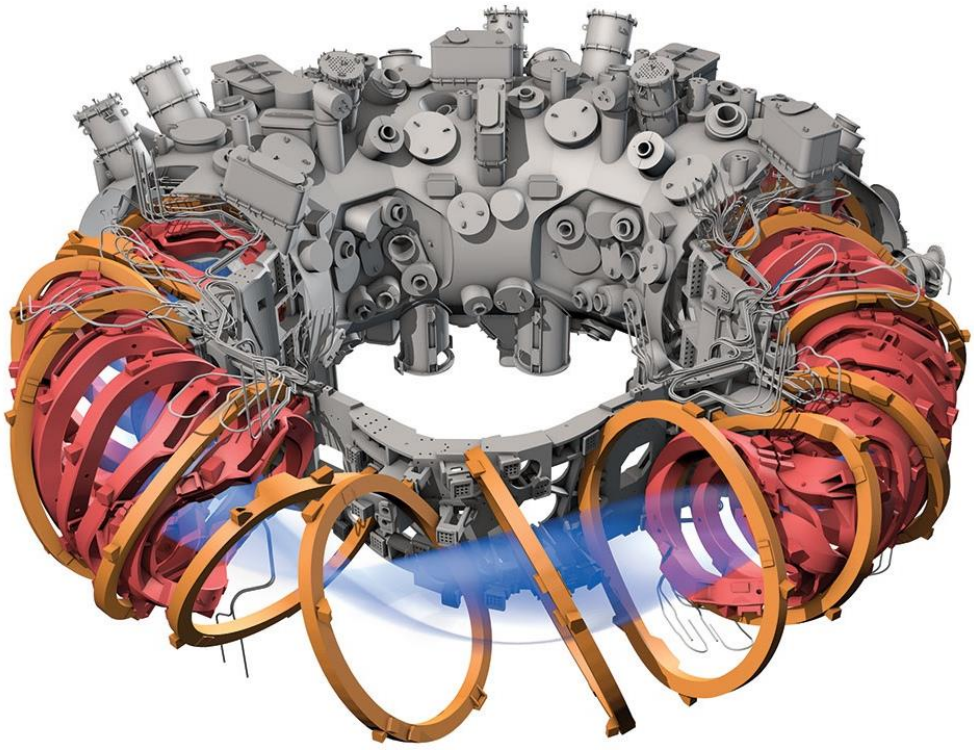

Figure 2. Schematic CAD drawing of Wendelstein 7-X (©IPP) [3]

In the case of a stellarator such as Wendelstein 7-X [4] shown in Figure 2, the plasma is confined in a magnetic field in the form of a twisted toroid, which causes the particles to rotate along this twisted path. This structure can attenuate the plasma instability that appears in the pure toroidal structure [5]. The tokamak device, which is the research subject of this paper, will be explained in more detail in the following.

1.1.2. Tokamak and Magnetic Field Configuration

Tokamak devices have been studied for about 70 years as the most promising way to realize fusion energy. The doughnut-shaped device confines the plasma with a magnetic field, which must maintain the temperature of hundreds of millions of degrees that the particles must reach for nuclear fusion over a long period of time. To this end, a strong magnetic field in the toroidal direction is applied from the centroid coil in the device. As the plasma particles flow along this strong magnetic field, the magnetic field gradient and its curvature cause ∇B drift motion up or down depending on the charge the particle has. An electric field is formed by this charge separation, and the plasma could escape the device in an outward direction by the $E \times B$ drift motion. Therefore, to prevent such charge separation, a toroidal direction plasma current is induced by a poloidal direction coil. This results in a helical magnetic field structure and forms a magnetic flux surface. When this magnetic flux surface is viewed in

the poloidal plane, various magnetic field configurations can be identified. This magnetic field configuration affects the plasma confinement and its performance, as well as the holding power of the device.

Among them, the most studied magnetic field configuration, "Divertor configuration" has the core plasma from the boundary plasma surrounding it. This boundary plasma is called Scrape-Off Layer (SOL), and has an open flux surface unlike the core plasma with a closed flux surface, and transports particles and heat flux transferred from the core to the divertor. The magnetic flux surface between them is called a separatrix or the Last Closed Flux Surface (LCFS). In the divertor configuration, one or two magnetic field null called X-point inevitably exists and is located on the separatrix. According to the number and location of the X-point on the separatrix, Lower Single Null (LSN), Upper Single Null (USN), and Double Null (DN) configurations can be distinguished as shown in Figure 4. In addition, the DN can be classified more according to the distance from the outer midplane (OMP) of the flux surface of the two X-points. This distance is called dR_{sep} as shown in figure 1. In general, if this dR_{sep} is smaller than the Larmor radius of the ion, it is classified as Balanced DN (B-DN). If it is between the Larmor radius and the SOL decaying length, which is the exponential decaying length of the particle or heat in the SOL OMP, it is unbalanced DN (UB-DN), and if it is larger than the decaying length, it is classified as SN [6]. In the KSTAR (Korea Superconducting

Tokamak Advanced Research) device, this Larmor Radius, and SOL decaying length are similar [7], so DN can mean B−DN.

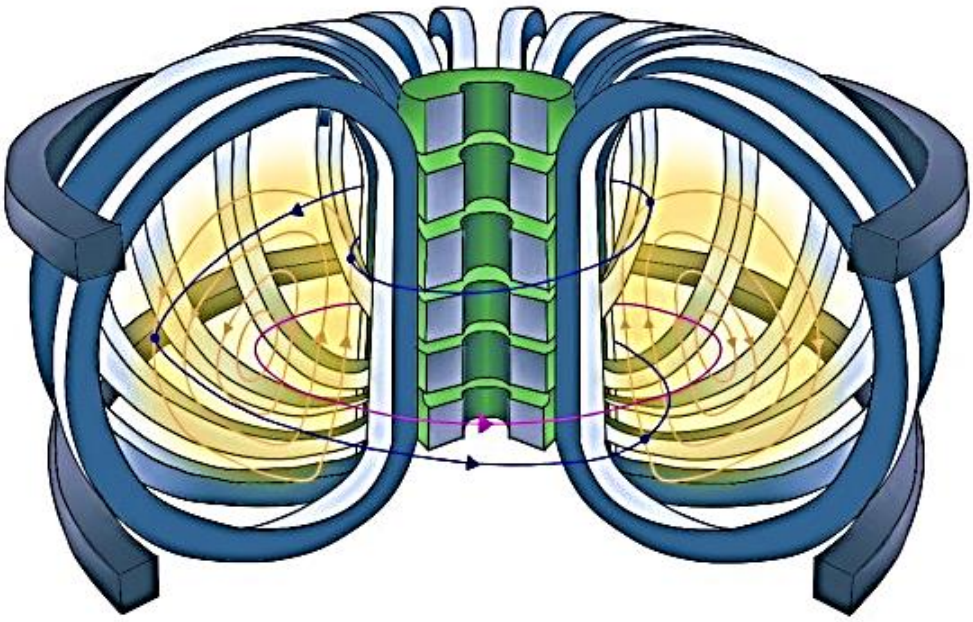

Figure 3. Schematic figure of tokamak device and magnetic field configuration.

In such divertor configurations, when the power of a certain value or more is applied to the plasma from the external sources, an "L−H transition" in which performance in an edge region of the core plasma dramatically increases occurs, and a high confinement state, so−called "H−mode", may be entered. This power value is called threshold power, P_{th}, and may be different for each device and plasma condition. As shown in Figure 1, many experiments have shown that when the direction of the magnetic field is the ▽B drift

motion toward the active X-point, the L-H transition occurs at a lower P_{th} than the opposite direction. In this case, the former case is called a "favorable" configuration, and the latter is an "unfavorable" configuration.

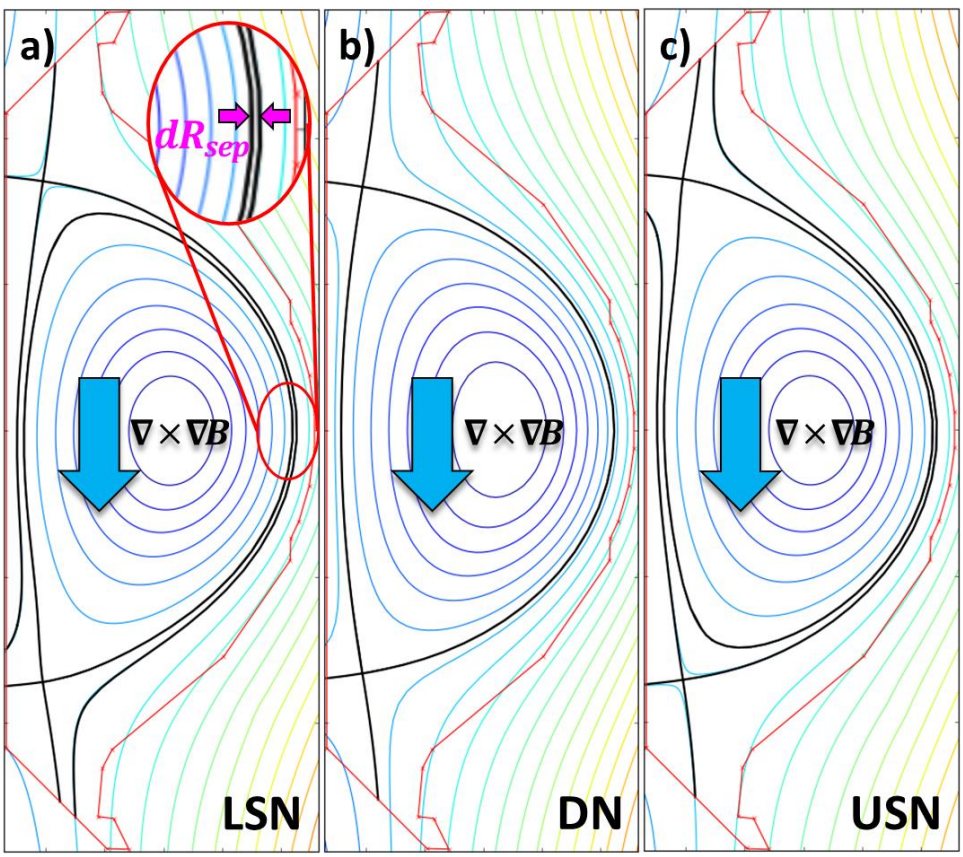

Figure 4. Magnetic field configurations in KSTAR and definition of $\mathbf{dR_{sep}}$. a) favorable LSN, b) DN, c) unfavorable USN configuration. The red circle highlights the gab between two magnetic surface that passes the two X-points.

1.1.3. Merit of Double Null Configuration

Among the DN, the Balanced Double Null configuration has various advantages. First, since the shape of the core plasma of DN is closer to a triangular shape, the stability and confinement of the plasma can be improved [8]. Due to the structural characteristics of the tokamak, the magnetic field decreases as the distance from the central axis of the torus. In this magnetic field gradient, it is advantageous for the plasma confinement that the particles stay a little longer in a place where the magnetic field is strong. Here, High Field Side (HFS) means a half domain of the tokamak where the magnetic field is stronger than the magnetic axis. The other half domain is called the Low Field Side (LFS). Therefore, the shape of the core plasma is very important because it determines the path of the plasma within the magnetic field configuration. This "plasma shaping" is controlled by parameters such as triangularity and elongation, and studies have been conducted to find the optimal plasma shaping parameters to secure performance and stability [8], [9]. In this context, DN can have a larger triangularity than SN, so it has the advantage of having a larger shaping effect.

The second point is that the heat exhaustion problem can be solved more smoothly [10], [11]. In the divertor configuration, particles and heat fluxes coming out of the core plasma are transported to the divertor region through the SOL region. The flux surface with the same value as the separatrix extending to this

divertor is called the diverter leg, and the point where it touches the divertor is called the strike point. This diverting plasma heat flux, called divertor heat flux, usually has a peak value near this striking point, and its distribution varies depending on the degree of cross-field diffusion in the SOL region. For the commercialization of nuclear fusion reactors, it is important to design such that the peak value of this divertor heat flux does not exceed the engineering limit of the material. The DN configuration has a great advantage in this respect, which is that it can operate two outer divertors simultaneously. This means that the majority of the heat flux escapes from the LFS where the magnetic field is the weakest and the gradient is the largest in the core plasma, it is possible to distribute the heat flux to two outer divertor sides which have a larger area due to a larger major radius. In addition, the SOL transport in the LFS has a relatively very long reach to the divertor, resulting in a lot of cross-field diffusions, which can lower the peak value of the heat flux. Also, there is a possibility of securing a larger physical space to install a more advanced divertor.

The last advantage is that since the SOL region in DN is divided into HFS and LFS by the two X-points, the particle/heat exchange between the two regions becomes difficult. As mentioned above, most of the particle and heat fluxes escape through the LFS and expecting low cross-field diffusion in the HFS, very sharp SOL profiles are formed in the HFS. This makes the ideal location for the Radio Frequency (RF) actuators, which may suffer less plasma-

material interactions with reduced penetrated impurity in the core. Moreover, RF wave physics prefers the HFS [12].

From these advantages, B-DN is used in the design of many fusion reactors and DEMO concept devices, such as UWMAK-I [13], CIT [14], ITER CDA [15], ARIES-I through ARIES-ST and ARIES ACT [16]-[18], BPX [19], FIRE [20], K-DEMO [21], and ARC [22].

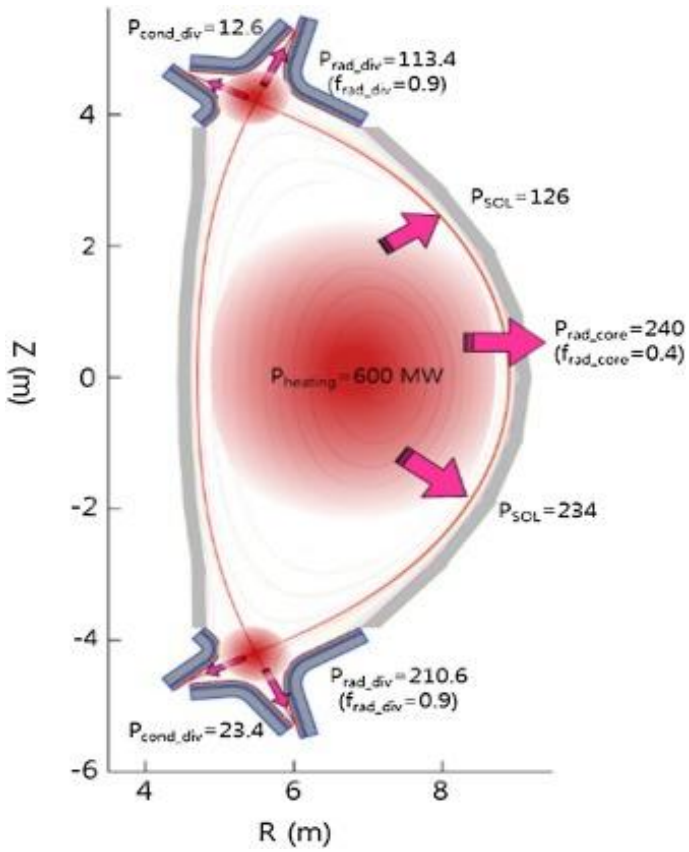

Figure 5. Plasma power flow diagram for K-DEMO (unit in MW) [21].

1.1.4. KSTAR Tokamak

Korea's medium-sized tokamak device, KSTAR [23], as its name suggests, has been in operation since 2008 as a device using superconductors (Figure 6). The device is designed for research and development of advanced steady-state operation in superconducting tokamak prior to research into the ITER device and future fusion devices. The main parameters of KSTAR are major radius R = 1.8 m, minor radius a = 0.5 m, the magnetic field strength at the magnetic axis is around 1.8 T and up to 3.5 T, and plasma current, I_p usually operates at 0.4-0.7 MA, but maximum 1.2 MA was reached. Strong shaping is possible up to elongation κ = 2.16 and squareness δ = 0.8 [24].

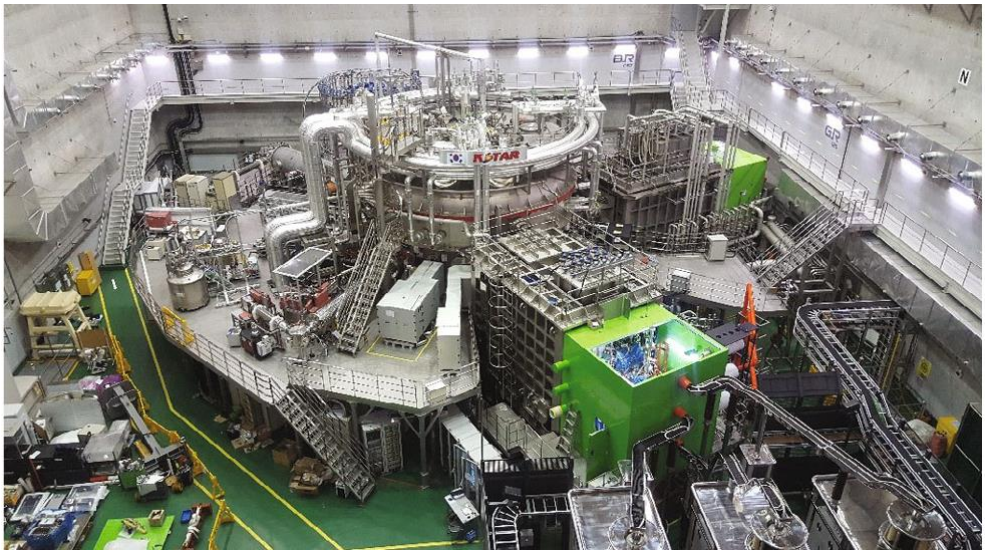

Figure 6. The bird eye view of the KSTAR device prior to the 2018 campaign [25].

Various advanced operation scenarios have been developed in the KSTAR. As major achievements, it maintained a high β_p-mode for up to 90 seconds in close to steady-state conditions, reached the high-performance plasma condition through the 'hybrid' operation scenario, and conducted high l_i operation scenarios to obtain a peaked plasma current profiles to get the high performance ($\beta_N = 3.0$) and the fusion gain [26], [27].

In particular, it has set a record of maintaining long pulses of 40 seconds without crashes of a magnetohydrodynamic (MHD) instability called Edge-Localized Mode (ELM). This record was achieved by controlling the ELM crash by forming ergodization of the magnetic field mainly in the edge region using an externally-induced small perturbation of the equilibrium magnetic field called Resonant Magnetic Perturbation (RMP). In the case of KSTAR, the design of producing the magnetic field is so sophisticated that its error is about one order smaller than other devices, so observing the effect of RMP is very effective [28]. Through this, it was possible to set a window model for the ELM-free area, and more efficient ELM control was possible [29].

In the design of KSTAR, the target H-mode operation time is set to 300 seconds. As a result of observations in the H-mode long pulse experiments so far, three limitations have been pointed out to achieve this goal [30]. The first is that the temperature of the PFC material, such as the diverter or the wall of the device, is not controlled. This is because the cooling rate applied to the PFC of KSTAR is currently

insufficient compared to that of the heat source from the plasma, so a steady state has not yet been reached for the temperature in this respect. Next, there are nonlinear drifts of the Magnetic Diagnostics (MD) such as the Rogowski coil, magnetic probes, flux loops, etc. Errors in these diagnostic devices can cause real-time control errors and lead to plasma performance degradation over a long period of time. Thirdly, gradual plasma performance degradation was consistently observed in long-pulse operations.

KSTAR is scheduled to be upgraded to a tungsten diverter with a larger heat capacity in 2023, and together with this, it will try to solve the PFC temperature limit by reducing the heat on the PFC through continuous shaping control optimization. The drifting problem of MD was artificially feed-forward controlled in the opposite direction of drift to reduce the drift error. This showed a clue to solving the problem to some extent, but it did not solve the essential problem, and the influence of other problems was not attenuated. Finally, in the case of performance degradation, various causes can be provided, such as impurity accumulation or gas pump control differences due to the accumulation of magnetic configuration control errors, similar to the magnetic diagnostics drift discussed above.

More than 50 diagnostic systems have been installed including improved basic diagnostics and advanced imaging diagnostics in KSTAR [31]. Among these diagnostics and magnetic diagnostics, there are Rogowski coils (RCs) that can measure plasma current, and arrays of Mirnov coils (MCs) are distributed poloidally and toroidally

to identify MHD mode numbers. In addition, Beam Emission Spectroscopy (BES) is a diagnosis that enables selective observation of local plasma ion density fluctuations in the corresponding region by observing fluctuations in the intensity of Doppler-biased Balmer series light emitted when a neutral beam is heated by high-temperature plasma. In other words, this device is designed to measure fluctuations of the order of $\frac{\delta n_e}{n_e} < 1\%$ of the mesoscale belonging to the frequency range of 0.1~1.0 MHz [32]. As such, BES is used as an important means of measuring and diagnosing edge fluctuations caused by plasma turbulence.

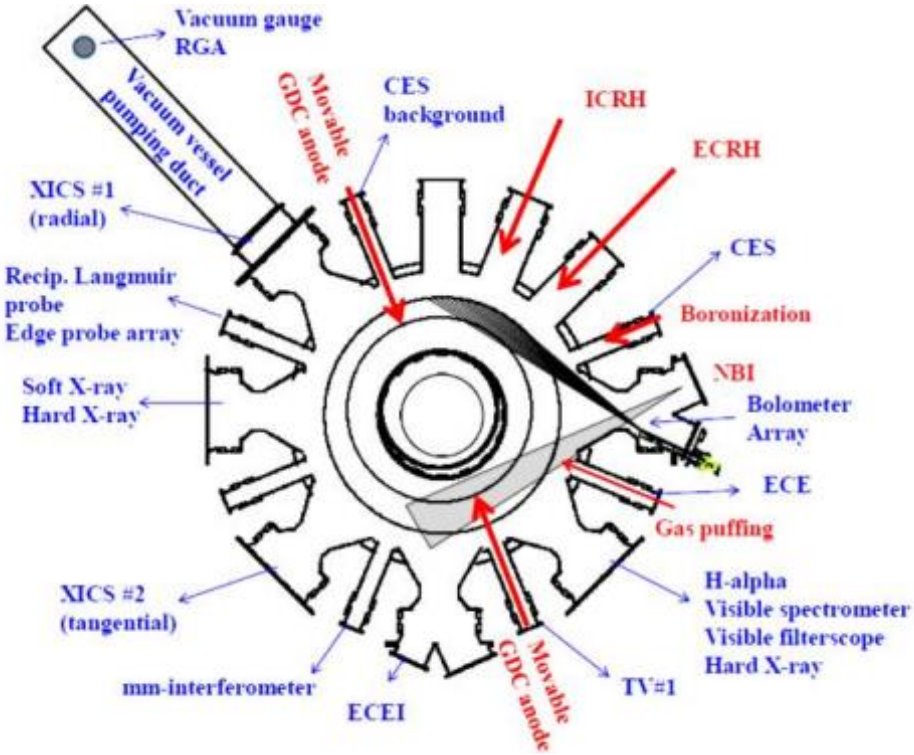

Figure 7. Top view of the KSTAR including main diagnostics, heating systems, and wall conditioning systems [33].

The IR-visible Two-Color Interferometer, a diagnostic device that observes light interference by using the difference in the path of light from the same light source, consists of existing two legacy single-chord systems and 5-chord, it is used to find tangential line-densities of electrons [34], [35]. The Thomson scattering device, which can measure the temperature and density of electrons by measuring photons scattered by free electrons in plasma, has been continuously updated since its installation in 2009, with a total of 31 measurement points and a time resolution of 20 to 50 Hz [36]. In the case of ion temperature, KSTAR has installed and used Charge Exchange Spectroscopy (CES). This diagnosis method measures the temperature and rotational speed of plasma ions using a spectrum generated when neutral particles derived from Neutral Beam Injection (NBI) for plasma heating collide with impurity ions. More specifically, impurity ions excited through charge exchange emit a spectral line, and by calculating Doppler broadening, Doppler shift, and their area, the temperature, rotational speed, and density of impurities can be obtained, respectively. At this time, in order to measure only the light caused by the charge exchange, KSTAR modulates NBI to unveil the background light and subtract it [37].

1.2. Motivation

To compare the shaping effect of these magnetic field configurations, 35 SN to DN transition experiments are performed in KSTAR. These experiments started with a favorable LSN H−mode "hybrid" operation mode to the DN by gradually adjusting the $\mathrm{dR_{sep}}$. The "hybrid" operation scenario is developed as an advanced inductive scenario with higher confinement and greater stability [26]. The range of $\mathrm{dR_{sep}}$ is −2 cm to −1 cm for LSN, then it increases toward 0 cm for 1 to 2 seconds.

In these DN transition discharges, the plasma current is in the 0.6~0.7 MA and external heating power from the Neutral Beam Injection (NBI) is in a range of 3.5~4.8 MW. These experiments have no significant MHD instabilities that may degrade the plasma performance such as kink mode or tearing mode.

In many of these discharges, it was observed that the plasma performance increased as the density decreased. Plasma performance is represented by the normalized beta ($\beta_N = \beta/(I_p/aB_T)$) and the normalized confinement time ($H_{89} = \tau/\tau_{98}$). Here β is the ratio of the plasma pressure to the magnetic field pressure, I_p is the plasma current, a is the plasma minor radius, B_T is the toroidal magnetic field strength, τ is the energy confinement time, and τ_{98} is the IPB98 confinement scaling relation. These changes occurred gradually according to $\mathrm{dR_{sep}}$ changes and were maintained for a

considerable period of time after the transition ended. The reason for this gradual increase in performance is expected to be due to the increased fast ion by NBI as the density decreases [38]. This will be explored in more detail through an example discharge in the following.

1.2.1. Density Pump-out During DN transition

The examined KSTAR discharge is shot 25460 as shown in Figure 8. As dR_{sep} changes from −1.4 cm to 0 cm, it can be seen that the plasma boundary changes from favorable LSN to DN. In the meantime, β_N and H_{89} rose by more than 25%, the line−averaged electron density decreased from 4.5 to 4.0, and the electron temperature increased from 4.0 keV to 5.45 keV. And the plasma safety factor at the edge q_{95} and the neutron rate from the fission chamber also increased gradually according to the dR_{sep}. Lastly, the deuterium (D) α emission intensity signal (D_α) shows a reduction in its intensity and changes its frequency after 8.4 seconds when dR_{sep} passes around 0.3 cm.

A preliminary study suggests two reasons for the performance improvement in the discharge. First, due to the decrease in the density of plasma ions, more fast ions can remain due to the low collisionality from NBI, resulting in increased contents and increased performance. This can be seen from the gradually rising neutron rate.

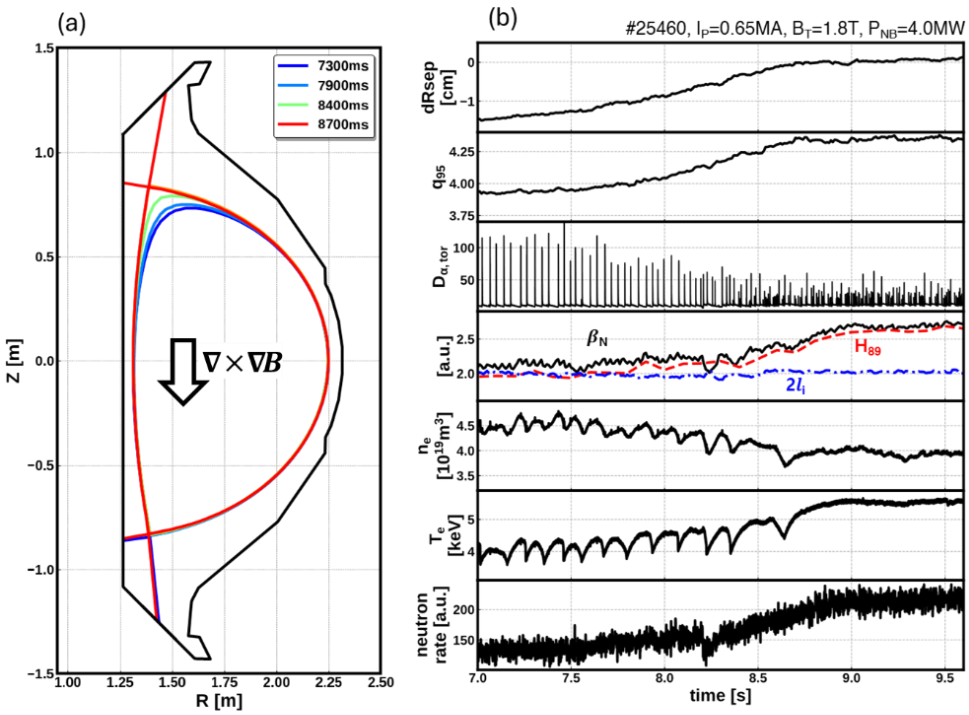

Figure 8. KSTAR DN transition discharge; Shot 25460. (a) The Last Closed Flux Surface (LCFC) during shaping control from LSN (7300 ms) to near DN (8700 ms). (b) Time evolutions of the discharge. Boxes from top to bottom: $\mathbf{dR_{sep}}$ (cm), $\mathbf{q_{95}}$, toroidal $\mathbf{D_\alpha}$ signal, plasma 0-D parameters ($\boldsymbol{\beta_N}$, $\mathbf{H_{89}}$, **and** $\mathbf{l_i}$), line-averaged electron density, electron temperature at the center, and

Second, the stability boundary is changed due to the shaping effect that changes as it transitions to DN, resulting in higher performance. In H-mode, as mentioned before, an MHD instability is likely to occur due to the high-pressure gradient near the edge transport barrier. An optimum in plasma performance is achieved by a careful balance between good confinement properties and MHD stability [39]. ELM is one of these MHD instabilities and can be described as a periodic

repetition of ballooning (pressure-driven) and peeling (current-driven) modes, and their boundary is called a stability boundary. In DN transition, this stability boundary expands and has a more stable pedestal, the region where the edge transport barrier exists, resulting in improved performance. This can be seen through the fact that the distribution of the D_α signal that appears according to the occurrence of ELM changes its pattern to very grassy around 8.4 seconds, and the performance parameters rise more steeply.

In this study, the reason for the decrease in density mentioned in the first reason is addressed more closely to catch clues to the corresponding increase in plasma performance. The next, among them, the density pump-out caused by various fluctuation modes occurring near the edge pedestal region will be investigated and whether it can be applied to DN transition will be investigated.

1.2.2. Density Pump-out by various modes at the Edge Pedestal

In Tokamak plasma, various mode fluctuations occur in the core region. These modes can arise from macro- or micro-instabilities, and affect plasma parameters like density or temperature. These mode fluctuations usually coexist within a band. In the case of Coherent Modes (CM), the band is very narrow and is known to be generated from MHD mode or geodesic acoustic modes (GAMs) [40]. When such CM occurs, it is known that outward particle flux occurs between ELM crashes near the edge, but the mechanism is not yet

clear [41].

Especially, among these CM, Coherent Edge-localized Mode (CEM) has been discovered. This mode has been found in the pedestal recovery phase of the normal type I ELM (big, periodic crashes) and noted as a major candidate for increasing particle and heat transport during this period. The pedestal broadening and continuous density decreasing may be occurred by CEM, which have been observed in a few high-performance KSTAR 'hybrid' scenario discharges [42].

Alternatively, Quasi-Coherent Modes (QCM) are found at a specific frequency band like CM, but the band is broader. As can be seen, it is thought to have occurred by interacting with the turbulence that is the background such as Trapped Electron Modes (TEM) or Ion Temperature Gradient (ITG). As in the case of CM, QCM also reduces the ion density by generating particle outward flow with E×B convection between the crash of the ELM [43].

Also, Edge Harmonic Oscillation (EHO) mode, which appears in Quiescent H-mode (QH-mode), provides continuous particle and impurity transport crossing the edge transport barrier. Edge rotation or edge rotation shear is the variable of these EHO-driven particle transport [44].

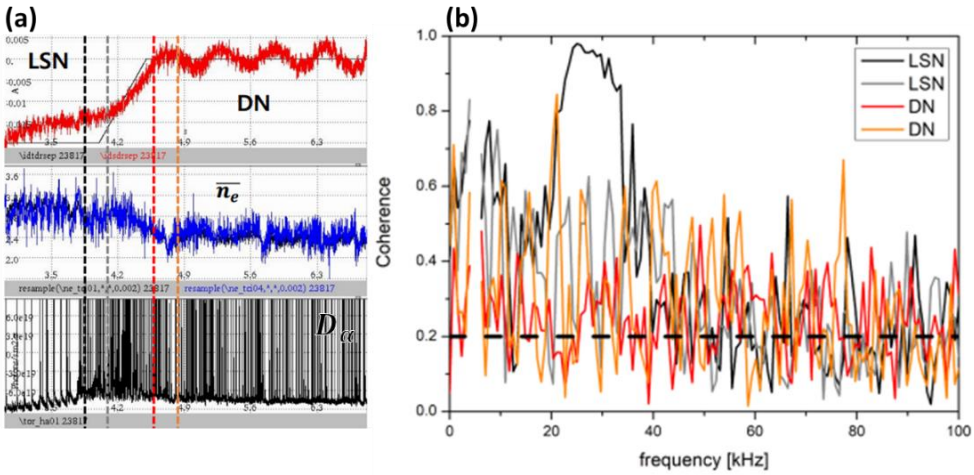

Figure 9. KSTAR DN transition discharge; Shot 23817. (a) Time evolutions of the discharge. Boxes from top to bottom: $\mathbf{dR_{sep}}$ (cm), line-averaged electron density, toroidal $\mathbf{D_\alpha}$ signal. (b) mode coherence parameter in the frequency of each time slice.

These modes occur frequently in plasma discharges and are highly likely to exist in KSTAR discharge shot 25460 analyzed in this paper. However, it is estimated that the observed density decrease has other reasons besides these mode effects. First, no clear MHD mode was observed, and second, it was due to the KSTAR discharge shot 23817 shown in Figure 9. In this discharge, the coherent mode that occurred in the favorable Lower Single Null (LSN) state was significantly attenuated right before the transition, and the DN transition proceeded. As the density decrease is observed even in the DN transition where the fluctuation mode does not exist significantly, a phenomenon that affects the density pump-out linearly according to the $\mathrm{dR_{sep}}$ change to explain this is needed.

1.2.3. Possible Three Reasons

In this dissertation, three expected reasons are suggested as the cause of the decrease in density as the dR_{sep} gradually changes.

(1) Difference in recycling due to the changing SOL structure

In SN, the connected SOL shares the outward particle and heat fluxes from the core plasma. These fluxes divert to the inner and outer divertor each with a comparable portion of half of the total amount. On the other hand, in DN, the SOL in the HFS is separated by the X-points, which only take about 30% of the total outward flux from the core plasma. This difference of the diverting fluxes near the inner divertor, very roughly 50 % vs 15%, can lead to the gap of the particle fueling by the inner divertor recycling between the magnetic field configurations. In addition to this, KSTAR usually has a very short inner divertor leg compared to the outer divertor, the recycled particle can easily transport to the core pedestal region to source the density. It is expected that this inner divertor recycling can reduce the density by reducing the core density fueling effect in DN as the effect changes linearly according to the DN transition process.

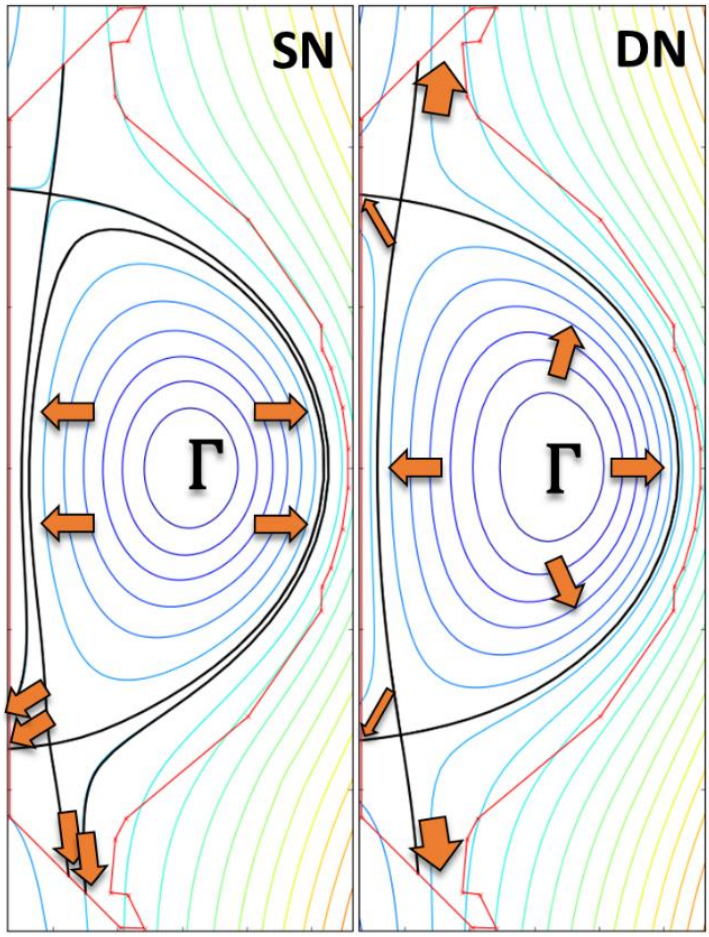

Figure 10. A schematic cartoon represents the particle flows in the SN and the DN.

(2) Changing of the ▽B drift due to the additional X−point

There are many studies that the direction of the ▽B is related to the height of the density pedestal [43]−[46]. Sontag et al. [46] studied this effect by the SOLPS−ITER [47], [48] simulation with respect to the position of the active X−point of the SN configuration. In this paper, the ▽B drift is added to the reproduced simulation model of

both favorable and unfavorable SN configurations. These additional ▽B drift−driven radial fluxes pump the density out to the separatrix convectively in both the favorable and the unfavorable cases. In this paper, they proposed that the difference in the pedestal height between the favorable and unfavorable H−mode discharge comes from the difference in the amplitude of the ▽B drift−driven radial flux.

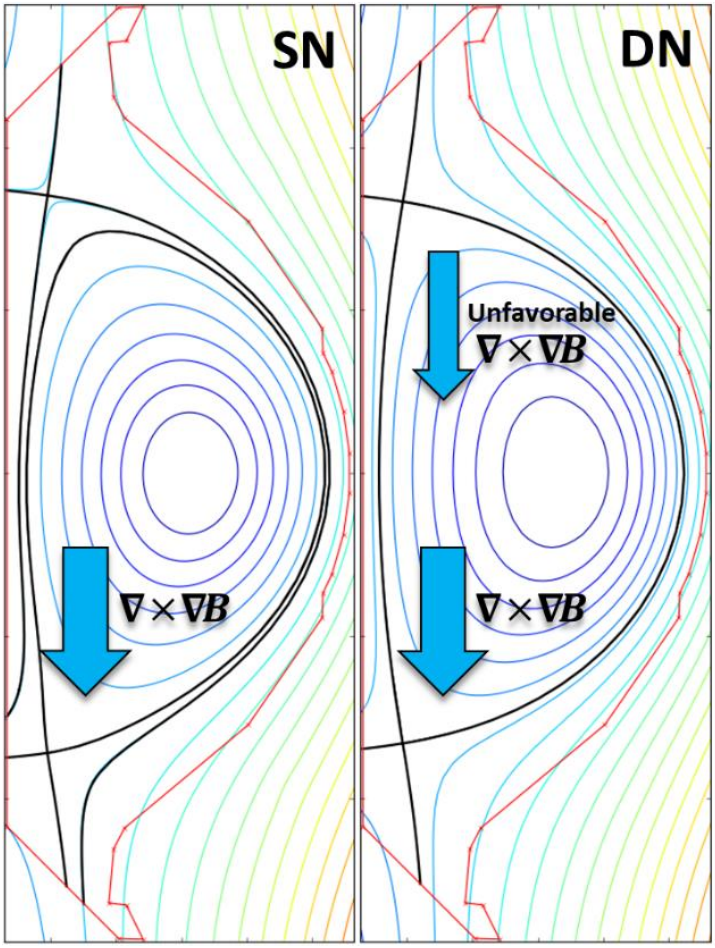

Figure 11. A schematic cartoon represents the assumption of the effective particle flows of ▽B drift in the SN and the DN.

Here, the question comes out. What about the ▽B drift effect on the DN configuration, which has both favorable and unfavorable X−points? As shown in Figure 11, it is expected that these B drift−driven fluxes can coincidently occur not alternatively placed during the change of magnetic field configurations. In this sense, a stronger ▽B drift−driven convection may pump out the density in the DN configuration. This expectation can also be applied to the gradual changes in the DN transition.

(3) Additional out−flow due to the E×B drift in SOL

Most of the SOL transport researchers point out that E_θ ×B drift makes the SOL flow to the inner divertor from the outer divertor near the active X−point in a favorable ▽B drift direction [45], [49], [50]. This particle flow accelerates the recycling near the inner divertor which pumps up the pedestal density. In the case of DN, the same phenomena happened, but, the E×B drift−driven flows are opposite near the additional X−point, a formal inactive one as shown in Figure 12. The oppositely directed flux pumps out the plasma and the impurities to the outer divertor in which the gas outlet is located. These later flows can decrease the isolated HFS SOL density leading to the low recycling condition in that SOL region. Since this phenomenon can occur during the SOL region between X−points narrows, it is thought to be able to explain the gradual density

decrease that occurs in the DN transition.

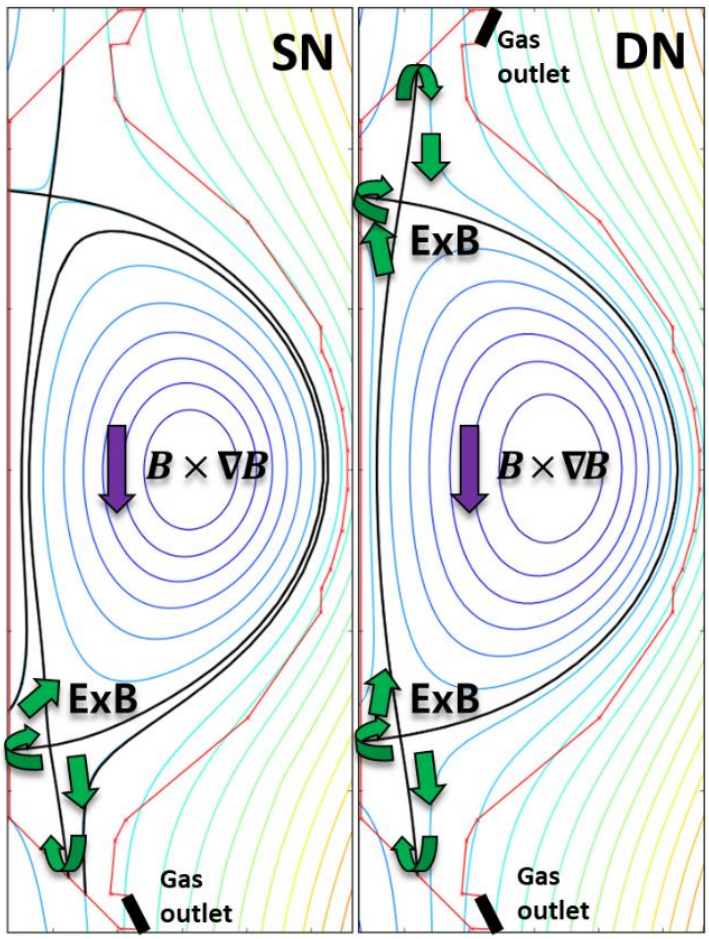

Figure 12. A schematic cartoon represents the direction of the ▽B drift and the particle flows of the E×B drift near the divertor in the SN and the DN.

1.3. Plasma Transport Modeling

Plasma exhibits a movement with various mechanisms such as turbulence, diffusion, and convection along its unique magnetic field structure in the tokamak device. This 'transport' of plasma is very important to improve the confinement and stability of the tokamak device, but the mechanism is very complex and difficult to understand with a simple formula. In addition, since the three possible reasons presented above are complex and integrated two-dimensional physical phenomena, it is clear that there are limits to studying those by experiments one by one. Therefore, in this study, mathematical models and numerical simulations are used to interpret these proposed hypotheses.

1.3.1. Modeling approaches

The following two modeling techniques are widely used to describe tokamak plasma.

- Kinetic Model

  It describes the motion of individual plasma particles by solving the Vlasov equation [45] as shown in equation (1.1), which includes the interactions between particles, and with the magnetic fields in the tokamak.

$$\frac{\partial}{\partial t} f_a(\boldsymbol{x}, \boldsymbol{v}, t) + \boldsymbol{v}_a \cdot \frac{\partial f_a}{\partial x} + q_a(\boldsymbol{E} + \boldsymbol{v}_a \times \boldsymbol{B}) \cdot \frac{\partial f_a}{\partial \boldsymbol{v}} = 0 \qquad (1.1)$$

where $f(x, v, t)$ is a general distribution function of particles at the phase spaces of velocity spaces $\boldsymbol{v}$, coordinates $\boldsymbol{x}$, and given time t. And $\boldsymbol{E}(\boldsymbol{x}, t)$ and $\boldsymbol{B}(\boldsymbol{x}, t)$ represent the self-consistent electromagnetic field created in the point $\boldsymbol{x}$ at time moment t by all plasma particles. q_a is the electric charge of the particle $\boldsymbol{a}$. This approach is best suited for capturing the detailed behavior of the plasma and is used to study kinetic processes, such as instabilities, wave-particle interactions, and heating mechanisms.

- Fluid Model

  This approach treats the plasma as a continuous medium with macroscopic properties such as density, temperature, and velocity, which can be obtained from the experimental data. In this approach, the plasma is described by a set of fluid equations, such as MHD equations which consist of the conservation equations of mass, momentum, and energies. The fluid model is computationally cheaper than the kinetic model and is best suited for studying large-scale phenomena, such as plasma confinement, stability, and global behavior.

Using a kinetic model can produce very detailed and physically

accurate results, but it requires a lot of computational resources because the six-dimensional phase space of each particle must be calculated every time step along with their interactions. Therefore, the limitations are clear to describe the phenomenon that extends to the whole tokamak over a few seconds. Therefore, this study deals with numerical simulation using a fluid model.

1.3.2. Modeling Requirements

The above-mentioned reasons are hard to figure out one by one in the experiment because it occurs simultaneously in the SOL and core plasmas. Especially, density evolution is one of the challenging problems due to its inherent complexities such as gyro-motion or the motion with the drift, and turbulence behavior, collisional behavior, atomic reactions, gas puff/pump rate, etc. Therefore, to figure out whether the proposed reasons for the density pump-out are reasonable or not, a plasma modeling system is needed with the following constraints.

(1) Reliable Integration of the Core and SOL plasma modeling

Since 'fast ion' from the neutral beam injection in the core plasma is one of the main candidates for enhanced plasma performance, it is needed that the core plasma modeling reacts to the external sources.

In addition, in the case of the ▽B drift we expected, since it shows the effect as convection in the core plasma region, two-dimensional core plasma modeling is required to apply it. Above all, it is very important to be able to reliably solve the core plasma because what this study points out is the density pump-out in the core plasma.

And for the SOL plasma, the other two reasons are related to the inner divertor recycling, a robust modeling is needed. Because the perpendicular to the flux surface flow is comparable to that of the parallel to magnetic field flow, it is preferred to describe the SOL plasma as two-dimensional.

These two plasma regions are very distinguishable by their own characteristics such as the flow motions, the collisionality, impurity contents, and the magnetic field openness. However, eventually, there are connected through the separatrix, which means that they should provide a reasonable boundary condition to each other. There are many tries to this work, so-called "Integrated Modeling" such as C2 [46], JINTRAC [47], COREDIV [48], or the integrated code suites, which is a framework for the tokamak codes developed for each purpose. In these suites of codes, TRIASSIC [49], OMFIT [50], IPS [51], and CRONOS [52]. JINTRAC and COREDIV also use these frameworks, but, they are classified as an "Integrated Modeling System" in this dissertation since they are some sort of package for the purpose.

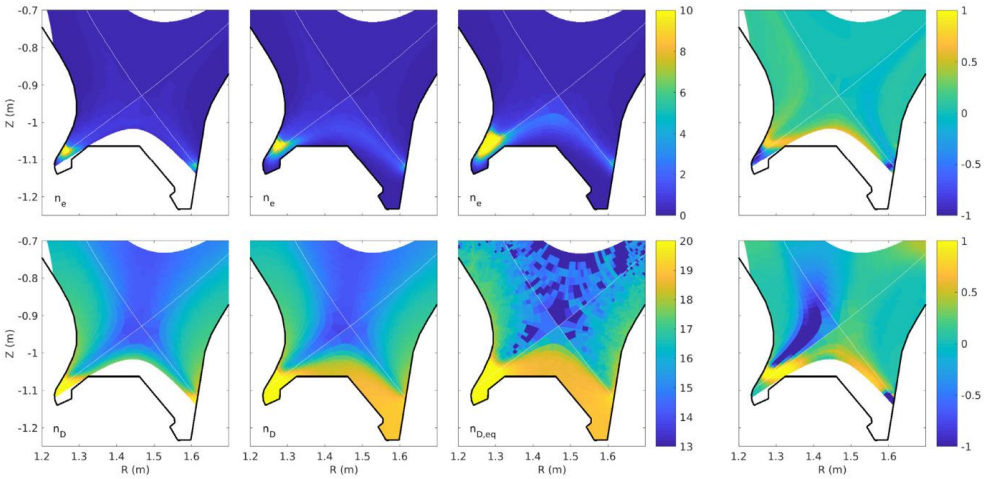

Figure 13. SOLPS-ITER simulation results of electron density (top) and neutral density (bottom) with respect to the extent of plasma computational grid [55]. (left to right) The target mode, the vessel mode, the vessel mode with kinetic neutral, and the relative difference between target and vessel mode solutions with fluid neutral.

(2) Broad Extent of the Finite Plasma Grid

The extent of the finite plasma computational domain should be chosen cautiously with the consideration of the SOL decaying length, λ_{SOL} [53]. Because, the numerical results are influenced by the grid extent, which determines the interaction range between the plasma and the neutral particles. The SOLPS-ITER, the state of art plasma boundary code package that is a combination of a 2-D multi-fluid plasma transport code B2.5 and the 3D kinetic Monte Carlo neutral transport code EIRENE [54], showed this dependency of the finite grid extent [53]. In the case of KSTAR, this grid extent is also very important for the simulation of the HFS and LFS SOL regions.

Because the two X-points are usually placed inside the KSTAR chamber, it should be chosen whether it includes the region near the inactive X-point as a calculation grid domain. Considering modeling the DN transition, it would prefer to include this inactive X-point area. This is because this region overlaps with the SOL of the DN.

(3) Realistic Wall Description

Likewise, considering the wall structure is important in this DN transition modeling. According to the wall description, the neutral particle distribution and the transport would be different and affect the plasma parameters such as the parallel flow [56]. This change in the flow also affects recycling and neutral transport. Especially, the inner divertor leg in KSTAR is very short compared to the outer, which makes the inner wall description important to the DN transition simulation in this device. In addition, considering the realistic wall description inevitably results in parts that are not aligned with the magnetic field. Therefore, boundary condition processing for these parts is also necessary.

(4) Inclusion of 2-D Drift Effects on the Both the Core and SOL Plasma

Two of the three reasons proposed in this paper are about the plasma drift perpendicular to the magnetic field. And ▽B drift effect is

expected to affect the core plasma convection, on the other hand, E×B drift effects would be occurred both in the core and SOL plasma. Also, both drifts have a term that is a cross-directional derivative, which could be a numerically challenging problem (orthogonality of the grid, interpolation scheme, flux conservation aspect, etc.). Furthermore, treating the electrostatic field can be difficult to converge, because the time scale of the electrostatic potential is shorter than that of the fluid-descript plasma simulation time scale.

(5) Other Requirements

For the other requirements, high accessibility to the simulation codes and modules is needed, good numerical convergence is prior due to the drift, high calculation speed is needed for the case study, and external module flexibility is for the magnetic field equilibrium or external heat source module.

1.3.3. Comparison of Integrated Plasma Modeling Systems

Table 1 shows the list of the integrated plasma modeling codes of systems that cover the region from the core/edge pedestal to the SOL with respect to the proposed modeling requirements. C2 [52] is the 2-D integrated code that covers the core and the SOL plasma, and JETTO-EDGE2D and COREDIV solve the core plasma as 1-D and are attached to the 2-D SOL solvers. UEDGE [63], SOLEDGE2D

[64], and SOLPS-ITER are plasma boundary codes whose simulation domain is from the edge pedestal region to the SOL region. C2 uses usually GTNEUT [65] as a neutral transport solver and the others use the ERIENE. All the plasma solvers can expand the grid extent, but UEDGE and SOLEDGE2D can cover the far SOL (near the wall) region. The boundary solvers are frequently used in the simulation with drifts.

	C2	JETTO-EDGE2D	COREDIV	UEDGE	SOLEDGE2D	SOLPS-ITER
Framework	IPS, TRIASSIC	JINTRAC	OMFIT			
Neutral Particle Solver	GTNEUT	EIRENE	ERIENE	ERIENE	ERIENE	ERIENE
Grid Extent	O	O	O	O	O	O
Realistic Wall Description	Implementable	X	X	O	O	Processing
Core-SOL Integration	Full 2D	1.5D Core 2D SOL	1.5D Core 2D SOL	2D EDGE-SOL	2D EDGE-SOL	2D EDGE-SOL
2D drift	Implementable	Difficult	Difficult	O	O	O

Table 1. Comparison various integrated modeling codes. C2 [46], JETTO-EDGE2D (JINTRAC [47]) and COREDIV (OMFIT[50]) are core-edge-SOL integrate modeling codes(system). UEDGE [78], SOLEDGE2D [79] and SOLPS-ITER [80], [81] are edge plasma solvers.

The 2-D plasma modeling system consists of the codes as follows. C2 is chosen in this study, because it covers the core and SOL plasma at once two-dimensionally, and can be implemented the required capabilities such as the 2-D drift and realistic calculation domain. The neutral particle transport solver, GTNEUT is also chosen, due to its calculation speed and compatibility with C2. VEGA2.0 is used as a grid generator and upgraded to provide the whole tokamak grid

for the realistic wall description. Lastly, the framework for these codes is TRIASSIC. A detailed description of the above codes will be introduced in chapter 2.

1.4. Outline of the Research

This research is focusing on the reasons for the gradual density pump-out during DN transition in KSTAR discharge. These reasons can be explained by the difference in SOL structure and core transport change according to the change in the magnetic field configuration. To this end, a modeling system that satisfies the requirements mentioned above was developed and elaborated on in the next chapter. Specifically, the combination of codes such as C2 and GTNEUT used in this modeling system and the extension method of the computational domain will be introduced in this chapter. Furthermore, the ∇B and the $E \times B$ drift are implemented and show the problems that occurred and how to solve them. Plus, the current continuity equation ported to obtain the E field is introduced, and the basic verification results of the developed modeling system are shown.

In Chapter 3, the developed modeling system was applied to the KSTAR #25460 experiment. In order to reproduce the discharge, the effective diffusivities under various conditions were first obtained

and compared with the fitting profile obtained in the experiment. Then, the difference between SN and DN was analyzed for the three reasons previously suggested for the observed particle diffusivity, and the reasonableness was judged by modeling each case.

In Chapter 4, the presented results were summarized, conclusions were made based on them, and future work was presented.

Chapter 2.
Development of 2-D Modeling System

2.1. 2-D Plasma Modeling System

In this chapter, the development of a 2-D plasma modeling system to model the DN transition in the KSTAR device is shown. First, the codes constituting the system are introduced, and then the process of improving the grid generator code for a realistic wall description is shown.

2.1.1. Core-Edge-SOL Integrated Simulation

(1) 2-D Plasma Solver: C2

As mentioned in the previous chapter, C2 is used as the main plasma transport solver. It solves the given two-dimensional computational

domain using the modified Braginskii' s fluid equations given by,

$$\frac{\partial n_i}{\partial t} + \nabla \cdot (\boldsymbol{b} \cdot n_i u_\parallel + \boldsymbol{r} \cdot n_i u_r) = S_{n_i} \tag{2.1}$$

$$\begin{aligned} m_i \left[\frac{\partial n_i u_\parallel}{\partial t} + \nabla \cdot (\boldsymbol{b} \cdot n_i u_\parallel u_\parallel + \boldsymbol{r} \cdot n_i u_r u_\parallel) \right] \\ = -\partial_\parallel (n_i T_i) - \boldsymbol{b} \cdot \nabla \cdot \boldsymbol{\Pi}_\parallel - \partial_r (\eta_r^a \partial_r u_\parallel) + S_m^i \end{aligned} \tag{2.2}$$

$$\begin{aligned} \frac{\partial}{\partial t}\left(\frac{3}{2} n_i T_i\right) + \nabla \cdot \left(n_i T_i \left(\frac{3}{2} \boldsymbol{b} \cdot u_\parallel + \frac{5}{2} \boldsymbol{r} \cdot u_r \right) \right) \\ + \nabla \cdot (\boldsymbol{b} \cdot q_{i\parallel} + \boldsymbol{r} \cdot q_{ir}) = Q_\Delta + S_E^i \end{aligned} \tag{2.3}$$

$$\begin{aligned} \frac{\partial}{\partial t}\left(\frac{3}{2} n_e T_e\right) + \nabla \cdot \left(n_e T_e \left(\frac{3}{2} \boldsymbol{b} \cdot u_\parallel + \frac{5}{2} \boldsymbol{r} \cdot u_r \right) \right) \\ + \nabla \cdot (\boldsymbol{b} \cdot q_{e\parallel} + \boldsymbol{r} \cdot q_{er}) = -Q_\Delta + S_E^e \end{aligned} \tag{2.4}$$

where the conservation of mass and momentum equations for the ion, and the temperature equations for both the ion and the electron, respectively. $\boldsymbol{b}$ represents the unit vector along the magnetic field line and $\boldsymbol{r}$ stance for the normal to the magnetic flux surface. n, u, T, and q are the density, velocity, temperature, and heat flux, respectively. And the subscript e, and i stance for the electron and ion, and $\parallel$, and r represents the parallel to the magnetic field, and the radial direction, respectively. m represents the atomic mass, $\Pi_\parallel$ is the parallel viscose stress, η_r^a is the radial anomalous viscosity, Q_Δ is the collisional heat exchange between ion and electron, and the

S_{n_i}, S_m^i, S_E^i, and S_E^e are the external/atomic source term for each equation.

Here, it is assumed that the anomalous diffusion is dominant in the radial direction,

$$n_i u_r \cong -D_p^{an} \frac{\partial n_i}{\partial r} \tag{2.5}$$

And Braginskii' s parallel viscosity is used in the parallel viscose stress $\eta_0 = 0.96 n_i T_i / \nu_i$, where the ion collision frequency is represented as $\nu_i^{-1} = 12\pi^{1.5}\epsilon_0^2 m_i^{0.5}(kT_i)^{1.5}/(n_i Z_i^4 e^4 ln\Lambda)$ with Coulomb logarithm $ln\Lambda$.

These governing equations of this version of C2 are simplified for public users, while the numerical schemes are the same. C2 uses the Finite Volume Method (FVM) with the SIMPLE-like algorithm. One of the strong points of this code is easily extendable the computational region by using the domain-deposition method. Through these advantages, it can provide results in the region of interest such as only core or SOL region, or coupled core-SOL region in the given magnetic field configuration. In this study, C2 solves the core plasma with the given radial transport coefficient and external sources, which are usually calculated at the magnetic flux surface, that are assumed to evenly distributed in the poloidal direction. This regulated the advantage of solving the core plasma two-dimensionally, however, it still has the distinctive two-dimensional features such as differences of the particle sources that

come from the 2-D SOL boundary and neutral transport. In addition, because the two plasma drifts dealt with in this study exist on the perpendicular plane to the magnetic field, this two-dimensional feature will become standing more out.

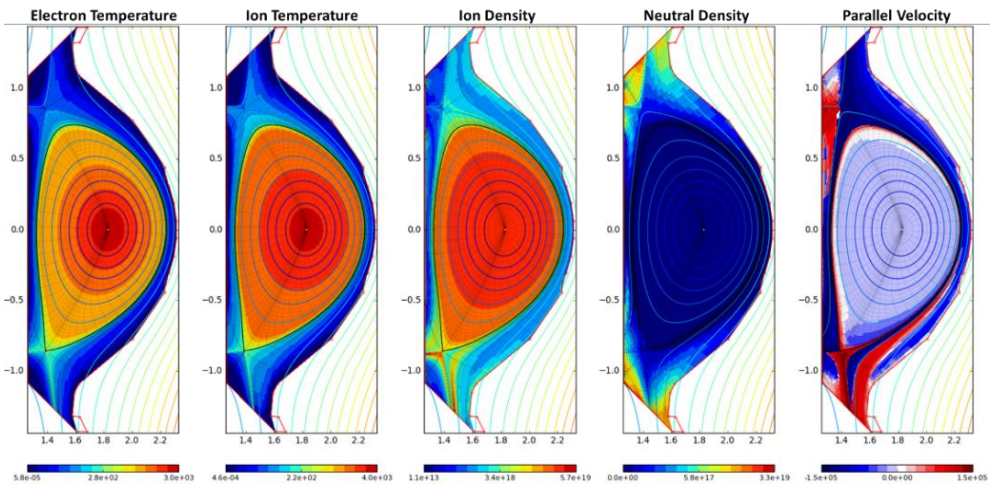

Figure 14. Example of the mesh plot of the KSTAR SN Discharge calculated by C2 and GTNEUT in the developed 2-D modeling system. (From left to right) Electron and ion temperature, ion density, neutral particle density (Deuterium), and parallel velocity of ion. The contour line represents the magnetic field equilibrium.

(2) 2-D Neutral Particle Solver: GTNEUT

GTNEUT uses the Transmission and Escape Probability (TEP) method in the given computational domain, which is subdivided into a number of cells. The partial currents J_{ij} from the ith cell to the adjacent j^{th} cell are calculated by balancing the transmission and

escape probabilities of each cell, which are preliminarily calculated by using first-flight integral transport methods. The neutral particle density at the jth cell can be obtained by

$$\frac{\partial n_n^j}{\partial t} = S_{ex}^j - \sum_k^j \left(J_{jk} - J_{kj}\right) - n_i^j n_n^j \langle \sigma v \rangle_{ion}^j + n_i^j n_i^j \langle \sigma v \rangle_{rec}^j \qquad (2.6)$$

where S_{ex}^j is the external neutral particle source and $\langle \sigma v \rangle$ stances for the cross-section for ionization or recombination. The superscript j means the value of the jth cell.

GTNEUT provides a steady-state solution of a neutral particle, Deuterium in this study, to the given plasma profiles. The result is comparable to the result from Monte Carlo methods with much shorter computational time because the probability table does not need to be recalculated unless the computational domain changes.

(3) Grid Generator: VEGA

For the purpose of the provide the grid suitable to the 2-D tokamak plasma solver using FVM, VEGA is developed [66]. It is a field-aligned quasi-orthogonal structured mesh generator that makes non-uniform grids by using the vector-following method, which uses the Runge-Kutta 4th order methods to draw lines along the magnetic flux surfaces. It finds the magnetic null points from the given magnetic field equilibrium and figures the magnetic field configuration

out within the limiter, SN, and B-DN (or Connected Double Null, CDN) by the number of the null points (X-point) and their locations.

VEGA is upgraded to VEGA2.0 for covering the other configurations UB-DN (or Disconnected Double Null, DDN) and generating the grid more automatically with keeping the orthogonality of the mesh. Through this upgrade, VEGA2.0 can generate a grid for the entire tokamak from the wall to the core region. More details will be given when the expansion of the plasma modeling domain is discussed in chapter 2.1.2.

(4) Framework: TRIASSIC

TRIASSIC (Tokamak Reactor Integrated Automated Suite for SImulation and Computation) [49]is used as a framework. It contains a group of interfaces for the plasma analysis codes targeting comprehensive interpretive and predictive tokamak simulations. As shown in the Figure 15, it uses IDS from ITER-IMAS as the internal data storage with various external modules such as equilibrium solver CHEASE [57] and FREEGS [58], external neutral beam injection solver NUBEAM [59], turbulent transport model TGLF [60] or GLF23 [61], and etc.

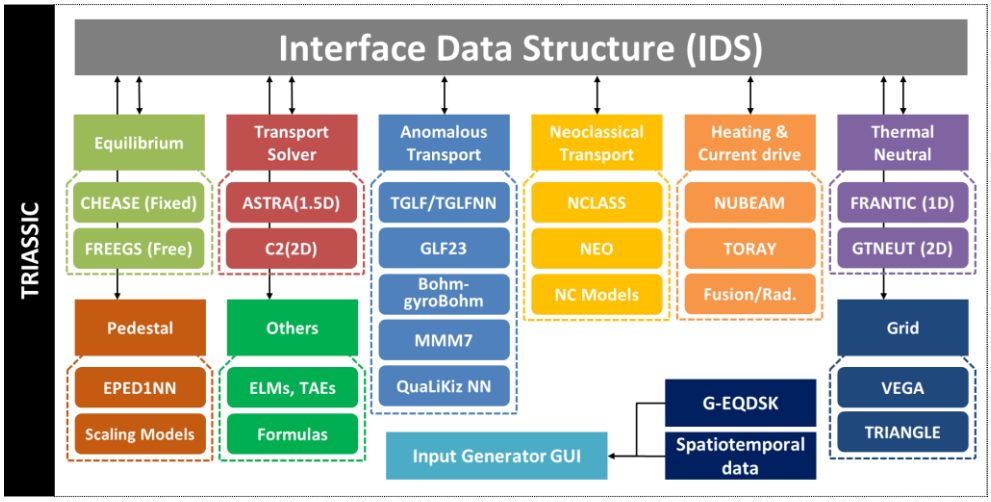

Figure 15. The schematic view of TRIASSIC integrated simulation framework [49]. TRIASSIC incorporates the interface data structure as its data storage, GUI which eases the input generation, and the plasma analysis code components.

Table 2. Summary of the codes used in this 2-D plasma modeling system.

Purpose	Code	Ref	Feature
Two-Dimensional Core-SOL Solver	**C2**	[46]	Modified Braginskii fluid model
Neutral Solver	**GTNEUT**	[62]	TEP
Grid Generator	**VEGA2.0**	[63]	Conformal Mapping
NBI	**NUBEAM**	[59]	Monte Carlo
Equilibrium Evolution	**CHEASE**	[57]	Fixed Boundary
Tokamak equilibrium	**EFIT**	[64]	Considering magnetic probe data (Magnetic-EFIT)

Table 2 shows the summary of what kind of codes are used in this 2-D plasma modeling system. Since TRIASSIC can give various options for the external modules, more codes will be used in later research such as the predictive simulation with the turbulent transport model or self-consistent pedestal modeling by the pedestal model module.

2.1.2. Expansion of the Plasma Modeling to the Wall

Grid Generation

Because of the flexibility in the calculation domain of the 2-D solvers, C2 and GTNEUT, generating the finite plasma grid is the key to the extension of the plasma modeling to the wall region. Therefore, as mentioned earlier, VEGA2.0 has been upgraded for this purpose. Grid generation proceeds in three processes. The first is to construct the frames of the domain by using the vector-following method, which is mostly divided by the magnetic flux surface passing through the X-point in the given tokamak chamber. And the last open flux surface can be drawn as the frames to close the flux tubes. These frames should be enclosed with other frames or device walls, and each domain must be quadrilateral for the later procedure.

The second is to section the created domains by plasma characteristics and numerical convenience. Practical domain names include core region, edge region, active SOL, active Private Flux

Region (PFR), Inactive SOL, Inactive PFR, and the wall region. The code automatically identifies the framed domains as above distinguishes its neighboring domains, and sorts the order of each quadrant counter-clockwise.

Finally, a conformal mapping method was used to form a mesh within the sectioned domains [65]. This method uses a function that locally preserves the angles and shapes, but not necessarily lengths. Therefore, if a Cartesian coordinate system with unit size length is used as a computational domain, it is possible to create a mesh grid that preserves orthogonality in a given quadrilateral. The function that converts from the computational domain to real geometry, $(\xi, \eta) \rightarrow (R, Z)$, is a Laplacian equation without the cross derivatives for the orthogonality, which is,

$$\begin{aligned} &\frac{\partial}{\partial \xi}\left(f\frac{\partial x}{\partial \xi}\right) + \frac{\partial}{\partial \eta}\left(\frac{1}{f}\frac{\partial x}{\partial \eta}\right) + P_x(h_\xi) + Q_x(h_\eta) = 0 \\ &\frac{\partial}{\partial \xi}\left(f\frac{\partial y}{\partial \xi}\right) + \frac{\partial}{\partial \eta}\left(\frac{1}{f}\frac{\partial y}{\partial \eta}\right) + P_y(h_\xi) + Q_y(h_\eta) = 0 \end{aligned} \tag{2.7}$$

where $P(h_\xi)$ and $Q(h_\eta)$ are inhomogeneous source terms that are the control parameters for the grid distribution. These two terms prevent the aggregation or twisting of the grid. h_ξ and h_η are the scale factors, which are equivalent to the distance of the sides. f is the distortion function defined as $f = h_\eta / h_\xi$. The discretization process, the iterative algorithm, and other details are described in

Ref [65]. An example of grid generation is shown in Figure 16. The red crosses represent the prepared quadrant input. This mapping procedure is conducted instantly and can control the grid distribution by $P(h_\xi)$ and $Q(h_\eta)$ terms, grid boundary conditions, and the convergence criteria.

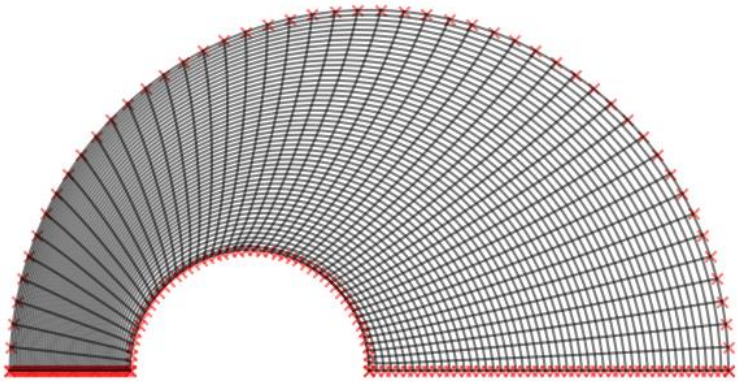

Figure 16. Example of the grid generation via conformal mapping method. The force constant is 0.1 and using sliding boundaries at the smaller circle. The red crosses are the input quadrant.

The example of the complete grid generated by VEGA2.0 for KSTAR SN discharge from the core to the wall is shown in Figure 17. In up and down gas outlet part is excluded from the grid generation because of the concave shape of the structure.

Update Boundary Condition

In the plasma transport solver, while updating the boundary condition at the wall, all sheath boundary conditions were updated to the

Bohm−Chodura sheath condition [66], [67]. When the magnetic field is not normal to the surface of the device, a Magnetic Pre−Sheath (MPS) is formed in front of the Debye sheath where a strong electric field is made by a sheath potential. A relatively strong electric field is also created in this MPS, and due to this, the plasma particles are accelerated so that the speed normal to the surface becomes sound speed ($C_s = \sqrt{\frac{T_e+T_i}{m_i}}$) at the edge of the Debye sheath. Also, in the Chodura−Riemann condition, it is said that the parallel velocity at the entrance of the MPS becomes this C_s. Therefore, this boundary condition is applied to the plasma governing equations with this MPS as the grid boundary.

With the introduction of these methods, it was possible to lay the foundation for operating simulations for the entire tokamak. However, a new problem arose: the grid generated near the wall is not aligned with the magnetic field and the resulting numerical problem of particle transport occurs. However, the effect of the problem caused by the wall plasma is very small due to the far distance from the main plasma. These problems and the solution will be discussed in the conclusion and future work.

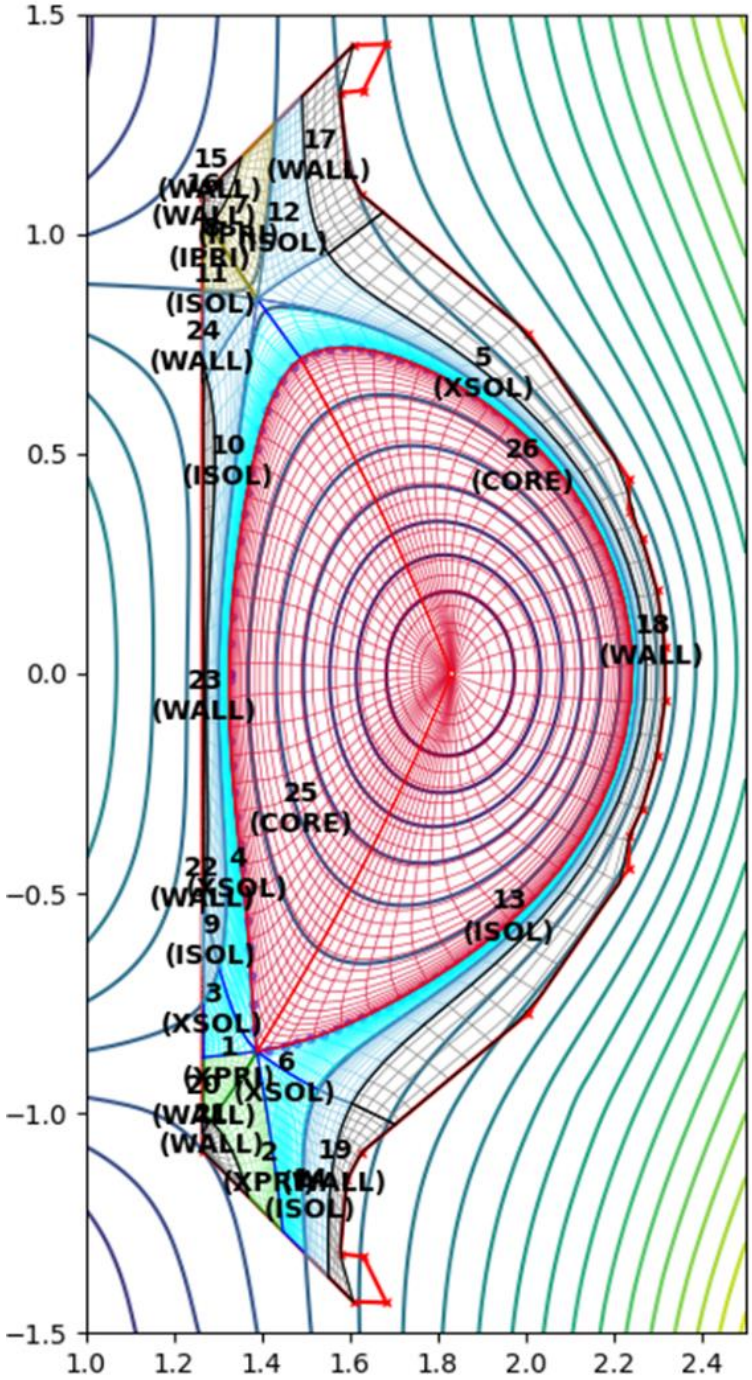

Figure 17. A computational grid system generated by VEGA2.0 covering the whole tokamak region. Each plasma region is distinguished by color; red for core plasma, cyan for SOL, blue for inactive SOL, green for the private flux region, and gray for the wall region. The number and text are the domain index and codes.

2.2. Implementing Drift Velocities

In order to simulate the reasons proposed in this study, both ▽B and $\mathrm{E} \times \mathrm{B}$ drift has been implemented in the C2, which version only had the parallel and anomalous radial velocities. Therefore, the drifts were derived according to the purpose of the study, implemented in the plasma transport solver properly to the FVM, and the problems that occurred were solved.

2.2.1. Theoretical Formulation

The plasma ion continuity equation can be written as

$$\frac{\partial n_i}{\partial t} + \nabla \cdot (\boldsymbol{b} \cdot n_i u_{\parallel} + \boldsymbol{w} \cdot n_i u_{\perp} + \boldsymbol{r} \cdot n_i u_r) = S_{n_i} \tag{2.8}$$

where $\boldsymbol{w}$ is the unit vector normal to both $\boldsymbol{b}$ and $\boldsymbol{r}$. (perpendicular or diamagnetic direction) The subscript $\perp$ stances for the perpendicular component.

The velocity components $u_{\perp}$ and u_r can be represented as drift and radial velocity from the anomalous radial diffusion flux.

$$\boldsymbol{w} \cdot u_{\perp} + \boldsymbol{r} \cdot u_r = \frac{\boldsymbol{B} \times \boldsymbol{\nabla}\phi}{B^2} + \frac{\boldsymbol{B} \times \boldsymbol{\nabla} p_i}{q n_i B^2} + \boldsymbol{r} \cdot \frac{1}{n_i} \Gamma_r^{an} \tag{2.9}$$

Where $\boldsymbol{B}$ represents the magnetic field, ϕ for the electrostatic potential, p_i for the ion pressure, q for the charge density, and the radial anomalous diffusion flux

$$\Gamma_r^{an} = -D_p^{an}\frac{\partial n_i}{\partial r} \tag{2.10}$$

where D_p^{an} is an anomalous diffusion coefficient.

The first term on the right-hand side of (2.9) is the $\mathrm{E}\times\mathrm{B}$ drift and the second term represents the diamagnetic drift. Utilizing the fact that the diamagnetic velocity is almost divergence-free, and avoiding the pressure gradients, using $p_i = n_i T_i$, where T_i is ion temperature,

$$\begin{aligned}
\nabla\cdot\left(\frac{\hat{\mathbf{b}}\times\nabla \mathrm{p_i}}{\mathrm{qB}}\right) &= \frac{1}{\mathrm{q}}\left(\nabla\times\frac{\hat{\mathbf{b}}}{\mathrm{B}}\right)\cdot\nabla \mathrm{p_i} \\
&= \frac{1}{\mathrm{q}}\left(\frac{1}{\mathrm{B}}(\nabla\times\hat{\mathbf{b}}) + \nabla\left(\frac{1}{\mathrm{B}}\right)\times\hat{\mathbf{b}}\right)\cdot\nabla \mathrm{p_i} \\
&= \frac{1}{\mathrm{q}}\left(\frac{1}{\mathrm{B}}(\nabla\times\hat{\mathbf{b}})\right)\cdot\nabla \mathrm{p_i} \\
&\quad + \frac{1}{\mathrm{q}}\left(\nabla\cdot\left(\mathrm{p_i}\nabla\left(\frac{1}{\mathrm{B}}\right)\times\hat{\mathbf{b}}\right) - \mathrm{p_i}\nabla\cdot\left(\nabla\left(\frac{1}{\mathrm{B}}\right)\times\hat{\mathbf{b}}\right)\right) \\
&= \nabla\cdot\left(\frac{\mathrm{n_i T_i}\hat{\mathbf{b}}\times\nabla \mathrm{B}}{q\mathrm{B}^2}\right) \\
&\quad + \frac{1}{\mathrm{q}}\left(\frac{1}{\mathrm{B}}(\nabla\times\hat{\mathbf{b}})\cdot\nabla \mathrm{p_i} - \mathrm{p_i}(\nabla\times\hat{\mathbf{b}})\cdot\nabla\left(\frac{1}{\mathrm{B}}\right)\right)
\end{aligned} \tag{2.11}$$

The last two term on the right-hand side of (2.11) is banished due

to the curvature of the magnetic field is out of interest in this study. The remained term of (2.11) is equivalent to ▽B guiding center drift of ions. So, the ▽B and $\mathbf{E}\times\mathbf{B}$ drift velocities are represented as,

$$u^{E\times B} = -\frac{1}{B}\frac{\partial\phi}{\partial\boldsymbol{r}}\vec{\boldsymbol{w}} + \frac{b_z}{B}\frac{\partial\phi}{\partial\boldsymbol{w}}\vec{\boldsymbol{r}} \tag{2.12}$$

$$u^{\nabla B} = \frac{T_i}{qB^2}\frac{\partial B}{\partial\boldsymbol{r}}\vec{\boldsymbol{w}} - \frac{T_i b_z}{qB^2}\frac{\partial B}{\partial\boldsymbol{w}}\vec{\boldsymbol{r}} \tag{2.13}$$

There are several problems in directly applying the derived drift to the numerical simulation. First, in the case of a region inside the core where the temperature is very high, the diamagnetic drift generated from the fluid approach may not be suitable for this regime. To be specific, a Coulomb collision of plasma is getting less effect on the particles as the relative velocity increase (high temperature). This makes the assumption difficult to apply that a continuous medium is formed by frequent interactions between particles. Second, the values of derivative terms may be unstable due to numerical inaccuracy. In particular, in the case of E×B drift, the value of the electric potential near the separatrix can fluctuate very drastically, and as a result, the numerical simulation can be greatly destroyed by an abnormal convection term from it. Therefore, in order to obtain more stability and keep the interesting physical phenomena, some practical procedure is needed and will be discussed in the next chapter.

2.2.2. Practical Implementation

In order for the drift derived from the fluid model to have a minimum physical meaning in the core region with high temperature as discussed above, the magnitude of the velocity in the corresponding direction should not exceed the component of thermal velocity. In order words, when defining the velocity due to drift as follows,

$$u_{\perp}^{d} = u_{\perp}^{E\times B} + u_{\perp}^{\nabla B} \tag{2.14}$$

$$u_{r}^{d} = u_{r}^{E\times B} + u_{r}^{\nabla B} \tag{2.15}$$

the effective drift velocities regulated by the thermal velocity can be defined as,

$$\tilde{u}_{\perp}^{d} = \frac{u_{\perp}^{d}}{1 + \frac{\left|u_{\perp}^{d}\right|}{v_{th}}} \tag{2.16}$$

$$\tilde{u}_{r}^{d} = \frac{u_{r}^{d}}{1 + \frac{\left|u_{r}^{d}\right|}{v_{th}}} \tag{2.17}$$

where the component of thermal velocity is represented as,

$$v_{th} = \left|\frac{B_p}{B}\right| \sqrt{\frac{8T_i}{\pi m_i}} \tag{2.18}$$

From the effective drift velocities (2.16) and (2.17), the ion continuity equation is updated as,

$$\frac{\partial n_i}{\partial t} + \nabla \cdot \left(\boldsymbol{b} \cdot n_i u_\parallel + \boldsymbol{w} \cdot n_i u_\perp^d + \boldsymbol{r} \cdot \left(n_i u_r^d + \Gamma_r^{an}\right)\right) = S_{n_i} \tag{2.14}$$

Likewise, the momentum equation is updated as,

$$\begin{aligned} m_i \left[\frac{\partial n_i u_\parallel}{\partial t} + \nabla \cdot \left(\boldsymbol{b} \cdot \Gamma_{i,\parallel} u_\parallel + \boldsymbol{w} \cdot n_i u_\perp^d u_\parallel + \boldsymbol{r} \cdot \left(n_i u_\perp^d + \Gamma_{i,r}^{an}\right) u_\parallel\right)\right] \\ = -\partial_\parallel (n_i T_i) - \boldsymbol{b} \cdot \nabla \cdot \boldsymbol{\Pi}_\parallel - \partial_r (\eta_r^a \partial_r u_\parallel) + S_m^i \end{aligned} \tag{2.15}$$

For the energy equations for the ion and electron, because the main interest of this study is the ion particle transport, this kind of implementation is not applied.

As implement drift, the boundary conditions are also updated considering the drift, using the Bohm−Chodura sheath condition. The parallel velocity at the boundary is calculated by using,

$$\boldsymbol{u}_\parallel \boldsymbol{b} \cdot \vec{\boldsymbol{n}} + \left(\boldsymbol{u}^{E\times B} + \boldsymbol{u}^{\nabla B}\right) \cdot \vec{\boldsymbol{n}} = |\boldsymbol{b} \cdot \vec{\boldsymbol{n}}| C_s \tag{2.18}$$

Through this relation, the heat fluxes for the ion and electron are also calculated.

2.2.3. Treating Cross-Directional Derivatives in FVM

Treating the drift velocities in C2 is different from the other velocities such as the radial anomalous velocity, due to the drift having the cross−directional derivative term to the velocity direction. In the finite volume, the sum of the fluxes through each cell face should be conserved. As shown in Figure 18, if all the plasma data is stored in the cell center in C2, then $\mathrm{E}\times\mathrm{B}$ drift velocity should be interpolated from the adjacent cells,

$$\begin{aligned} v_x^{E\times B}\Big|_e &= -\frac{1}{B}\frac{\partial\phi}{\partial y}\Big|_e \\ &= (1-g_e)\left(-\frac{\phi_N-\phi_s}{B\Delta y(N,S)}\right)+g_e\left(-\frac{\phi_{NE}-\phi_{SE}}{B\Delta y(NE,SE)}\right) \end{aligned} \tag{2.19}$$

where g_e is the linear interpolation coefficient, Δy is the distance between the points, and *N, S, NE, SE,* and *e* represent the north cell, south cell, north−east cell, south−east cell, and east side of the control volume *P*, respectively. In this consideration, the data of the control volume and its nearest neighbor don’t include, which makes a checkboard problem highlighted in Figure 19 (a).

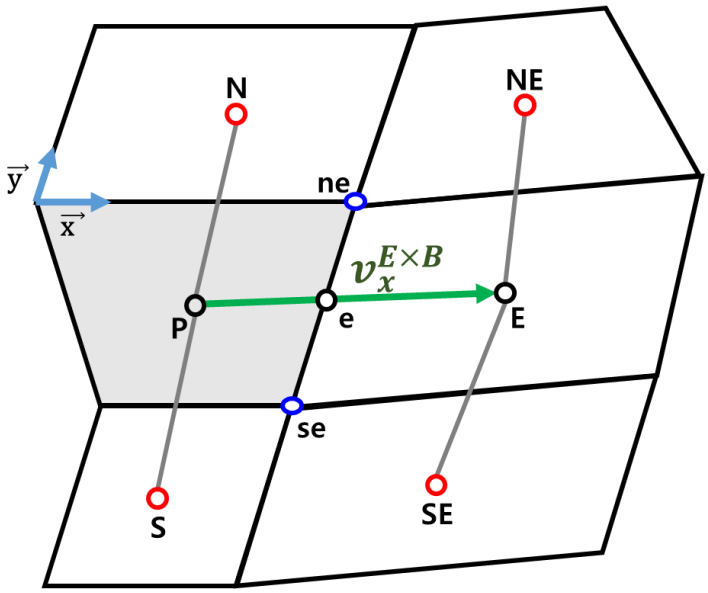

Figure 18. Schematic cartoon of the example for the consideration of $\mathbf{E}\times\mathbf{B}$ drift at the east side of the control volume.

In order to avoid this problem, Shepard's method [68] is introduced, which interpolates the given neighborhood data by normalization by the distance-related factor. End of each solution of plasma properties, the node data is calculated by the nearby 4-cell data (8 for the X-point). The $\mathrm{E}\times\mathrm{B}$ drift velocity at the east face is now simply calculated by,

$$v_x^{E\times B}\Big|_e = \left(-\frac{\phi_{ne}-\phi_{se}}{B\Delta y(ne,se)}\right) \tag{2.20}$$

The same consideration is applied to the ▽B drift.

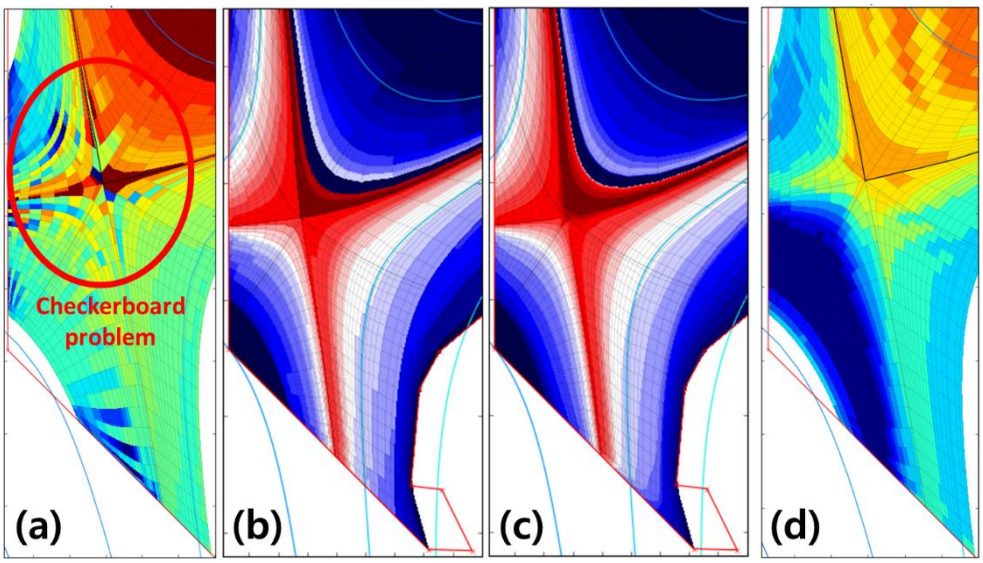

Figure 19. Example of 2-D mesh plots solving the checkerboard problem during c2 simulation including drifts. (a) Example of 2-D mesh plot ion density for the checkerboard problem due to using values at improper locations. (b) Example of cell data plot. (c) node data contour plot interpolated from the cell data. (d) Solved ion density mesh plot.

2.2.4. Implementing Current Continuity Equation

In order to calculate the electrostatic potential for $\mathrm{E} \times \mathrm{B}$ drift, a set of the current continuity equation are implemented in C2 from the UEDGE' s formulation [69]as follows,

$$\nabla \cdot (J_{\parallel}\boldsymbol{b} + J_{\nabla B}\boldsymbol{w} + J_{r}\boldsymbol{r}) = 0 \tag{2.21}$$

where,

$$J_{\parallel} = \frac{en}{0.51 m_e \nu_e}\left(\frac{1}{n}\frac{\partial n_e T_e}{\partial s} - e\frac{\partial \phi}{\partial s} + 0.71\frac{\partial T_e}{\partial s}\right)$$

$$J_{\perp} \cong \frac{2(n_i T_i + n_e T_e) + n_i m_i u_{\parallel}^2}{BR} \qquad (2.22)$$

$$J_r = e\left(\frac{1}{eB}\right)^2 \frac{\partial}{\partial r}\left(\eta_{\perp}^{a}\frac{\partial}{\partial r}\left(\frac{1}{n}\frac{\partial n_i T_i}{\partial r} + e\frac{\partial \phi}{\partial r}\right)\right)$$

$J_{\parallel}$, $J_{\perp}$, and J_r are the plasma current density components for the parallel, diamagnetic, and radial directions, respectively. Here, the diamagnetic current comes from the charge separation of the ▽B and curvature drift. In addition, the anomalous plasma current densities for both parallel and radial directions are introduced to diffuse the peak values for numerical stability.

The boundary condition for the divertor and the newly introduced wall region set as the sheath potential as like,

$$\phi_{sh} = \frac{T_e}{e}\ln\left(\frac{v_{T_e}}{2\sqrt{\pi}C_s}\right) = \frac{T_e}{e}\frac{1}{2}\ln\left[\frac{m_i}{m_e}\frac{2T_e}{T_i + T_e}\frac{1}{4\pi}\right] \qquad (2.21)$$

where v_{T_e} is an electron thermal velocity. For the core boundary, the fixed gradient boundary condition is applied, as known as the Neumann condition.

Figure 20 shows the example potential result calculated from the core to the wall region of the DN configuration with the fixed plasma

profiles. The radial potential and electric field are benchmarked with that of the SOLPS-ITER, which has a good agreement without the drift (results are not shown).

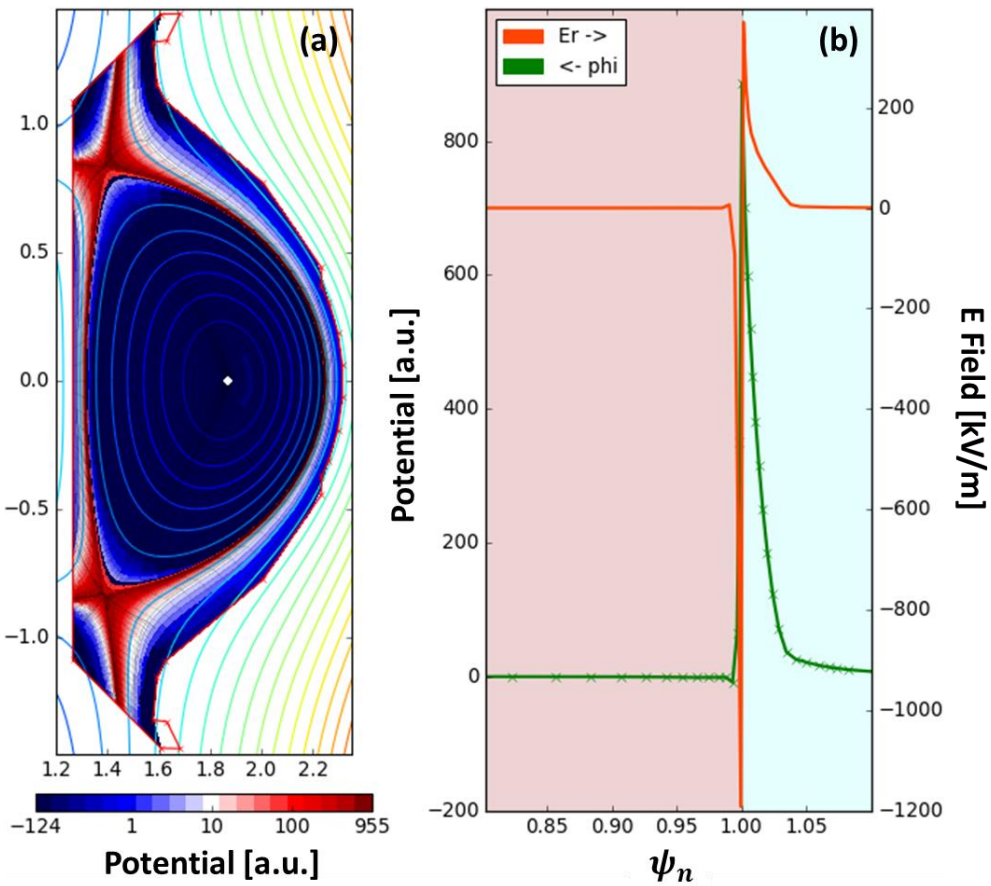

Figure 20. C2 calculated a two-dimensional electrostatic potential field. (a) 2-D contour plot of the potential field. (b) 1-D profiles of the potential (left) and electrostatic field (right) at the Outer Mid-Plane (OMP).

2.3. Verifying Developed Modeling System

The developed 2-D plasma modeling system is verified by benchmarking to the other conventional plasma simulation codes. Also, it compared the results with the experiment to try to validate this system.

2.3.1. Benchmarking with Other Codes

Figure 21 shows the benchmark results of the B2.5 (from SOLPS-ITER) and the developed 2-D plasma transport modeling system with the various grid configurations. The plasma properties set an artificially simple condition such as the fixed boundary condition at the core and SOL boundary and constant radial transport coefficients ($D_p^{an} = \chi_{i,e}^{an} = 1.0\ m^2/s$) everywhere. The results of the radial profiles at OMP for each grid configuration case agree reasonably.

This system is also benchmarked with ASTRA [70] in the given core plasma. With consideration of the parallel convection, the 2-D boundary effect at the separatrix makes difference near the edge pedestal region between the codes. However, the core plasma properties are matched well when the radial anomalous diffusivities are modified in that so-called "no man's land", edge pedestal region. This kind of modification is widely used in the interpretive simulation of SOL plasma.

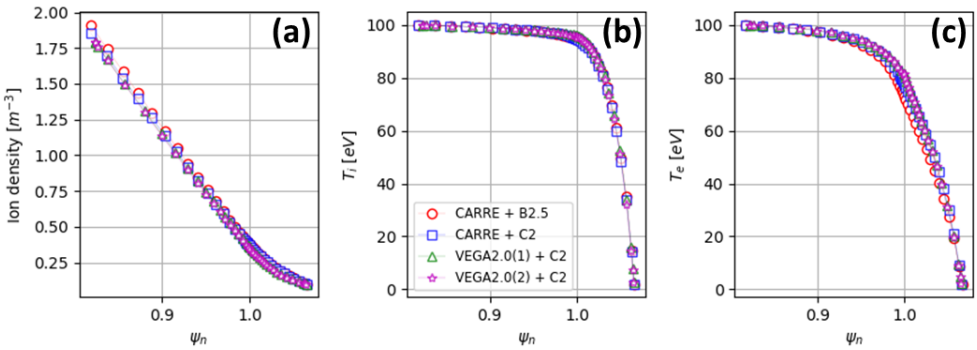

Figure 21. C2 benchmark to SOLPS-ITER code with various grids (CARRE, VEGA2.0(1), and VEGA2.0(2)). (a) Ion density, (b) ion temperature, (c) electron temperature.

The results of the neutral particle transport in KSTAR from GTNEUT are compared with that of EIRENE as shown in Figure 22. EIRENE is a component of SOLPS-ITER as a 3D Monte Carlo kinetic neutral transport code solving multi-species neutral transport including molecular reactions. The reaction equations used in a typical Deuterium plasma simulation in EIRENE are represented in Table 3. The reactions using in GTNEUT also in the table. The benchmark results show that the GTNEUT result is affordable compared to that of ERIENE when the same reaction equations are used.

Most importantly, in the case of GTNEUT, the calculations are surprisingly fast and reliable. In the case of the Monte Carlo method, it takes a very long time to obtain the converged profile from the ITER-scale tokamak. Therefore, it can be a very good tool when

conducting modeling experiments in various cases and identifying the tendency.

Table 3. Reaction table of the EIRENE Deuterium simulation. The red colored reactions are used in the GTNEUT

Species	Reaction
Atom (D)	$D + D(B) \rightarrow D + D(B)$ (EL) $D + D_2(B) \rightarrow D + D_2(B)$ (EL) $D + e \rightarrow D^+ + 2e$ (EI) $D + D^+ \rightarrow D^+ + D$ (CX)
Plasma (D^+)	$D^+ + e \rightarrow D$ (RC)
Molecule (D_2)	$D_2 + D(B) \rightarrow D(B) + D_2$ (EL) $D_2 + D_2(B) \rightarrow D_2(B) + D_2$ (EL) $D_2 + e \rightarrow D_2^+ + 2e$ (EI) $D_2 + e \rightarrow D + D + e$ (DS) $D_2 + e \rightarrow D + D^+ + 2e$ (DS) $D_2 + D^+ \rightarrow D^+ + D_2$ (EL) $D_2 + D^+ \rightarrow D_2^+ + D$ (CX)
Test ion (D_2^+)	$D_2^+ + e \rightarrow D + D^+ + e$ (DS) $D_2^+ + e \rightarrow D^+ + D^+ + 2e$ (EI) $D_2^+ + e \rightarrow D + D$ (DS)

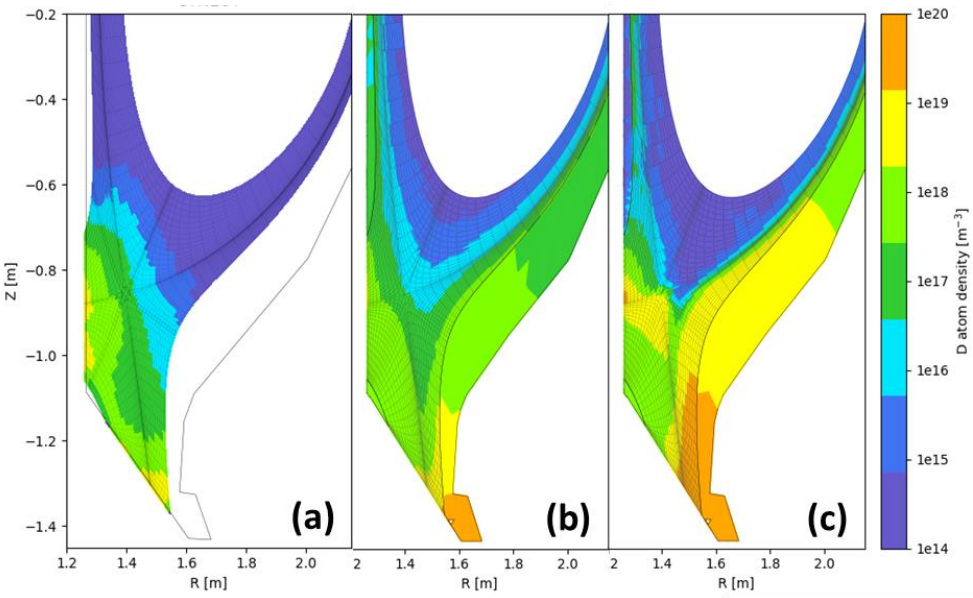

Figure 22. Benchmark GTNEUT to EIRENE. Neutral density from (a) GTNEUT, (b) EIRENE using D reaction only, and (c) EIRENE using same reactions with GTNEUT.

The further implementation of the reaction to GTNEUT is planned as future work when the impurity effects on the DN transition are considered.

2.3.2. Comparing with Experiment

The ELMy H−mode plasma discharge was reproduced by the developed 2−D modeling system. A detailed description for getting the experimental data and the simulation procedures will be introduced in the next chapter. As benchmarking the core plasma with the 1−D core plasma solver, the core profiles were set to the fitting data from the experiment, and SOL profiles were compared with

divertor heat flux as shown in Figure 23. As handling the control parameters such as anomalous cross-field diffusion coefficients in the SOL region, SOL plasma can be set as reasonable profiles fit with the experiment data.

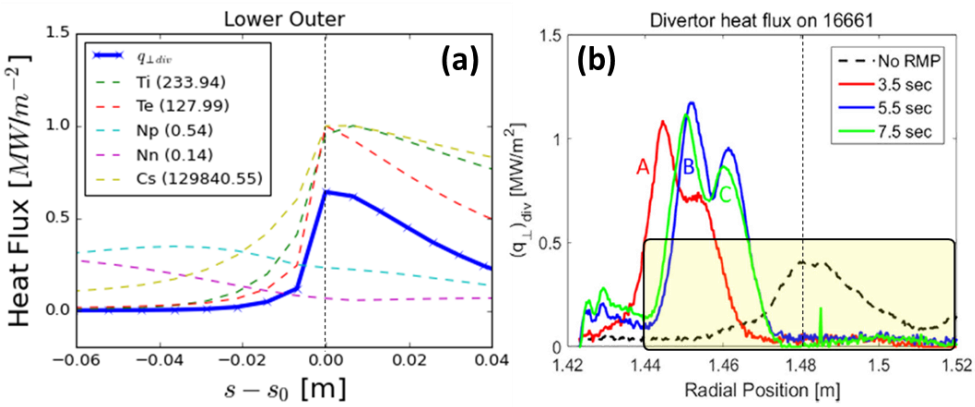

Figure 23. Divertor heat flux of a KSTAR H-mode discharge at the lower outer divertor; Shot 16661. (a) C2 simulation results. Blue for the divertor heat flux. (b) Divertor heat fluxes, the comparison target profile is a 'No RMP' case.

Chapter 3.

Application to KSTAR DN Transition Discharge

3.1. Modeling the KSTAR Discharge

In order to find out why the density is gradually pumped out in the DN transition, the plasma profile measured in the experiment must first be reproduced through the developed 2-D modeling system. And then, the profiles are going to be analyzed with the transport coefficient calculated through this modeled profile to infer the cause of density pump-out.

3.1.1. Preparation of the Modeling from Experiment

Diagnosis results in tokamak devices often involve some degree of

error or absence of data at the locations, and the plasma profiles must be established in consideration of these to ensure reliability in the following research. KSTAR device has a database system called MDS, and in order to construct a plasma profile, a desired shot and its time slice must be selected in this database. An accurate time slice is selected by collecting general information on the plasma through EFIT in a desired nearby time zone from the diagnosed 0D data. In this study, when selecting DN configuration data, as shown in Figure 24 (a), the time point when the two X-points are on the same magnetic flux line through EFIT was selected to exclude other obscure effects.

Also, when constructing the profile data, since ELM occurs in H-mode plasma periodically and the perturbation of the measured plasma profile is very large, the data near this time point should be avoided. In (b) of Figure 24, as one of the Graphical User Interfaces (GUI) of the GFIT tool [71], the data measured by CES is selected and placed for each time point in parallel with the D_α signal. In this study, in order to prevent the fluctuations caused by ELM, about 20% of the ELM cycle time after the ELM crash was avoided, and the measurement data after that time were collected. This is because it is known that about 90% of the pre-ELM value is recovered after 20% of the ELM cycle time [72].

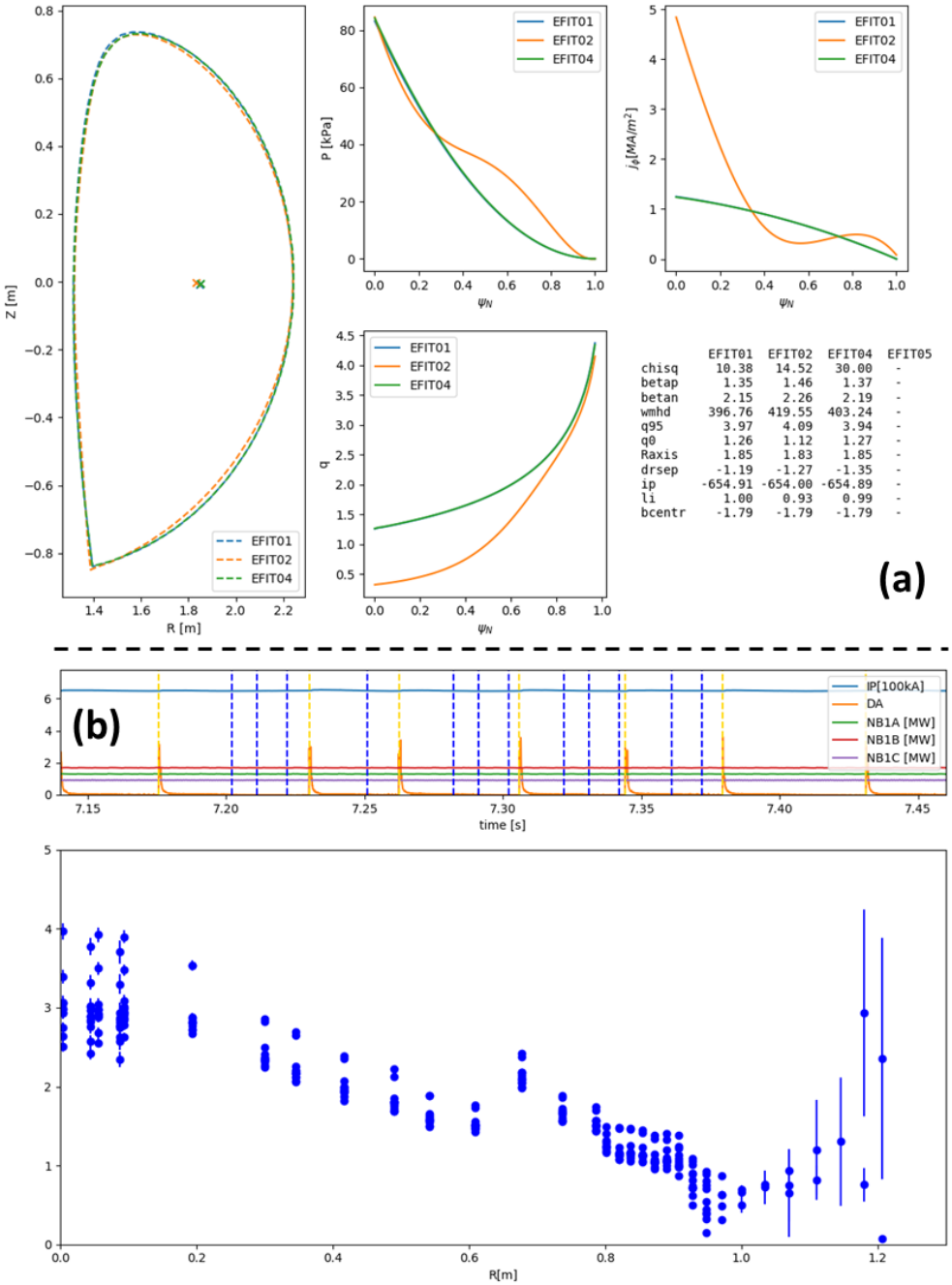

Figure 24. Experimental data acquisition from the measurement data KSTAR data server by (a) EFIT, (b) GFIT tool. The ELM timing and the data from the designated time slices are plotted.

The data acquisition has been conducted according to this procedure by using CES for ion temperature and toroidal rotation, Thompson Scattering diagnostics (TS), and Two-Color Interferometer (TCI) measurements for electron temperature and density. In Figure 25, the selected data and the fitted profiles are shown. These fitting profiles were constructed by applying the EPED model [73], and the pedestal width of the ion was used in the electron density and temperature pedestal width at this time for its accuracy and convenience. Some of the data, especially in the SOL, are not selected due to their high uncertainties. The values at the separatrix are used as free parameters to control the fitting accuracy.

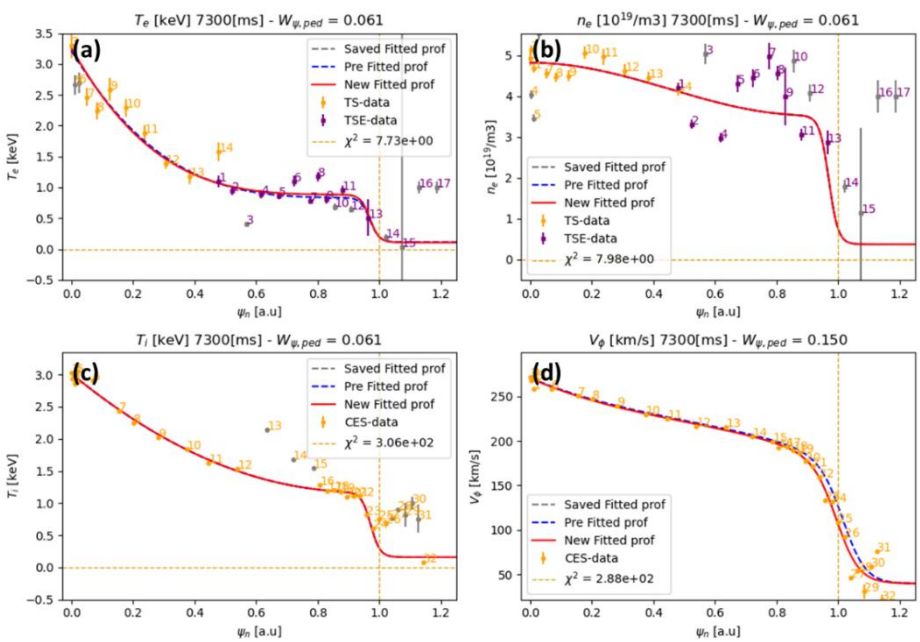

Figure 25. Measured data and the fitting profiles conducted in GFIT tool. (a) Electron temperature, (b) electron density, (c) ion temperature, and (d) toroidal rotation.

After the plasma profiles are constructed, it is needed to check their plasma stability. Figure 26 shows the j− α diagram conducted in the preliminary study [74]. This diagram represents the Peeling−Ballooning Mode (PBM) stability boundary in a $j_\phi - \alpha$ space, where j_ϕ is the edge current density, and α is the normalized pressure gradient defined in [75]. The constructed profiles are in the stable boundary of the blue dashed line of SN and the red solid line of DN. During the DN transition, the stability boundary is broadened, which means that the PBM becomes stable so that the DN can have higher pedestal pressure. This result agreed with that of the experiment. And the designated point with the error bar is the location where the constructed profile is placed in the $j_\phi - \alpha$ space. Both of the profiles are within the stable boundary, which means that the corresponding profiles are analyzable plasmas in a state where the ELM does not burst as intended.

With this, it was possible to obtain a plasma profile that could be used for modeling from the experiment and was used in later studies.

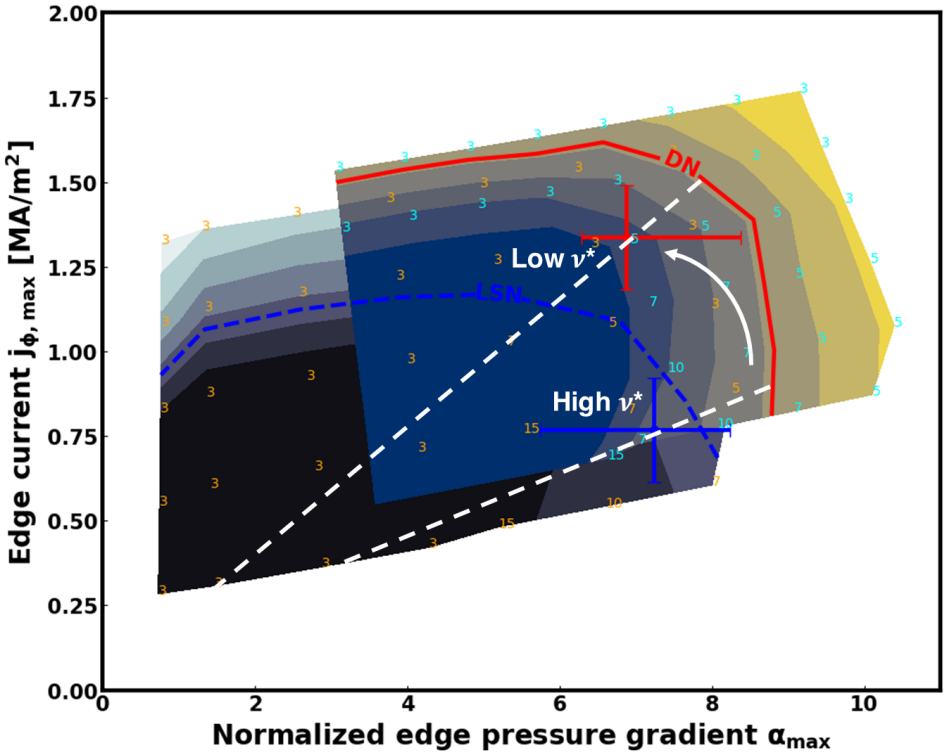

Figure 26. j-α diagram of the SN and DN configuration plasmas. The blue line stances for the stability boundary of SN and the red line for the DN. ν^* is the collisionality, and the low ν^* is for the DN due to the higher temperature and vice versa for SN.

3.1.2. Modeling the Kinetic Profiles without Drifts

The modules used for 2-D modeling were as already shown in Table 2. The process of constructing the steady-state 2-D plasma profiles is as follows. First, the effective diffusivities for the particle and energy, D_r^{eff} and χ_r^{eff}, in the core region are obtained through the given experimental core profile and external particle and heating source, which are calculated from NUBEAM in this study, by using,

$$D_r^{eff}(\psi) = -\frac{\int\left(S_{atomic}^i + S_{ext}^i\right)dV}{\oint \frac{\partial n_i}{\partial \psi} dS}$$

$$\chi_r^{eff}(\psi) = -\frac{\int\left(S_{atomic}^E + S_{ext}^E\right)dV}{\oint n_i \frac{\partial T}{\partial \psi} dS} \tag{3.1}$$

where ψ is the label for the magnetic flux surface, S is the surface area, and V is the volume. In the case of SOL plasma, a result converged to some extent for a given core plasma is used. For SOL diffusivities, $D_p^{SOL} = 0.1\sim0.5\ m^2s^{-1}, \chi_{i,e}^{SOL} = 0.1\sim2.0\ m^2s^{-1}$ is used and adjusted to match the separatrix value to the experimental fitting profiles or match the SOL diagnostic data. There are many ways to connect these two coefficients in separatrix, the boundary between the two domains, but in this study, a hyperbolic tangent function was used at a very short distance for simplicity.

Second, because there is a radial convective term such as the radial anomalous diffusion, it is necessary to converge so that the solution fits the given fitting plasma profile by using various variables. These variables basically include controlling the gas pump rate at the specified location (up and down the corner of LFS in KSTAR) or gas puff rate, the transport of neutral particle, controlling the flux limiter coefficient which regulates the parallel Braginskii flux to fit the low collisional regime, leveling the sheath transmission factor, and modifying the diffusivities at the edge pedestal and SOL region.

Finally, in the converged core and SOL profiles, each coefficient is fine-tuned to fit the commonly accepted experimental scaling parameters within the error bar of the diagnostic profile or the zero-dimensional parameters such as the total MHD energy. For example, in the case of SOL decaying length, particles in KSTAR have 1 to 3 cm, heat flux has 2 to 4 cm, and in this two-dimensional modeling, the gas pump rate installed in the device is adjusted to match those lengths.

The modeling profiles of SN and DN constructed in this way and their transport coefficients are shown in Figure 27. In these results, in the case of ion and electron temperatures, except for the difference due to the coordinates that depend on the magnetic field structure, no significant difference is found, if the diagnosis error is affordable in the profiles. However, in the effective particle diffusivity case, there is a large discrepancy is observed, even though considering diagnostic errors and other small variable differences. Here, it is expected that this large discrepancy occurred due to the difference in plasma profile. Therefore, another simulation is conducted that additionally applied the plasma profile of SN to the DN configuration to proceed with the same modeling process. As a result, the modeling applying the SN profile to the DN showed diffusivities similar to those of the SN (magenta line in Figure 28). This may seem obvious at first glance, but a detailed analysis is required to explain the difference between the two transport coefficients previously calculated.

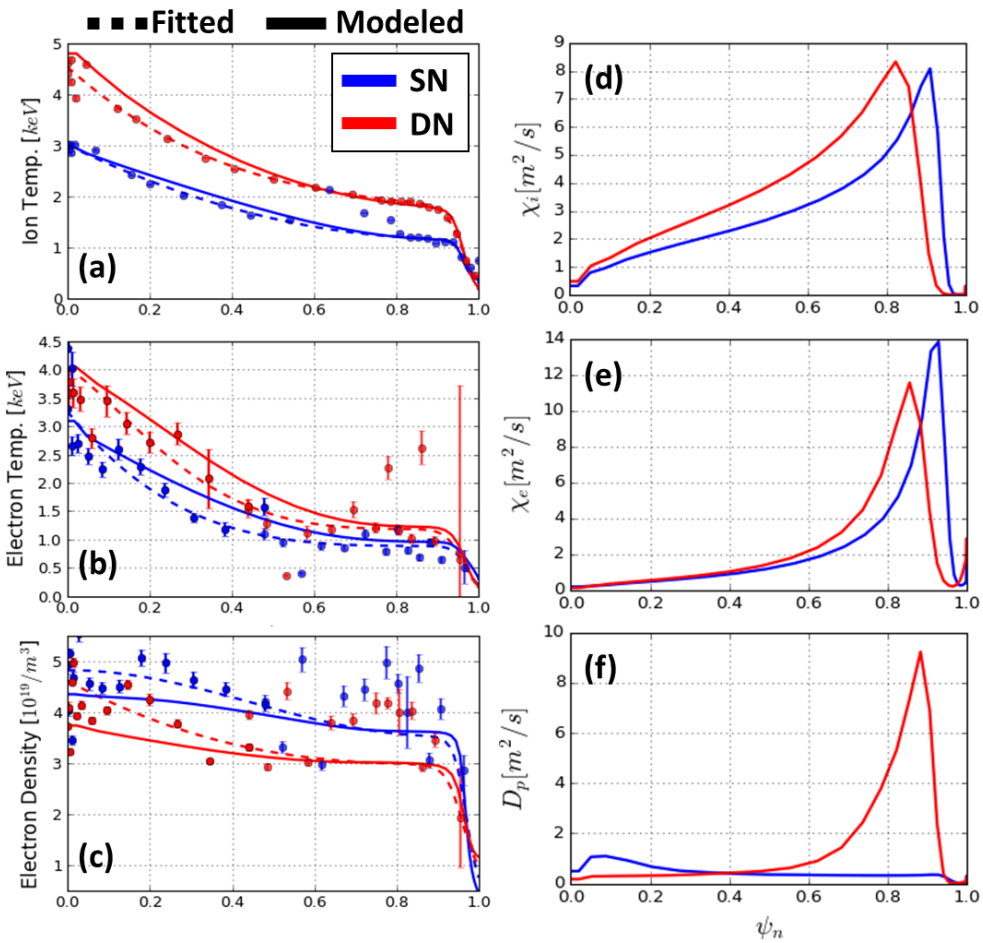

Figure 27. Reproduced plasma profiles of the KSTAR #25460 experiment. Blue for SN and red for DN, dotted lines for the fitting profiles from the experimental data, and solid lines for the modeled data. And the circles are the used measurement data. (a) Ion temperature, (b) electron temperature, (c) electron density, (d) effective ion heat diffusivities, (e) effective electron heat diffusivities, and (f) electron particle diffusivities.

3.1.3. Difference in the Particle Diffusivities of SN and DN

It might be an oversimplification, the difference in the particle diffusivities between the SN and DN is about 20 times (DN higher). Even considering inaccuracy from the diagnostics or the parameters for the profile fitting, these differences are very noteworthy. Therefore, in order to explain the large transport in the DN phase, especially near the edge pedestal region, some other effects should be suggested. As shown in Figure 28, it is expected that some sort of discrepancy comes from the three reasons proposed in 1.2.3. To connect the reasons to the analysis of the effective diffusivities, instead of using equation (3.1), the continuity equation in the steady-state is represented as,

$$\oint -D_r^{eff}\frac{\partial n}{\partial \psi}dS = \oint\left(\Gamma_r^{drift} + \Gamma_r^{an}\right)dS = \int (S_{ion} + S_{ext})dV \qquad (3.2)$$

where Γ_r^{drift} for the flux from the drift motion, Γ_r^{an} for the anomalous flux. Observations of each term in (3.2) with respect to the difference between SN and DN follow. The density gradient terms in the first term are dominant to decide the value of diffusivity and vary in the overall profiles, especially near the edge pedestal. And the last term becomes larger in the DN phase as indicated in the effect of NBI-driven fast ion heating, but the sum of the contribution of these two terms, the density gradient and the external source, is

not enough to explain the large discrepancy.

It is expected that the change of SOL flux between SN and DN can affect the ionization source term of the core plasma. On the other hand, the increased ▽B drift flux by combining the favorable and unfavorable flow in the core of DN would mean that DN has a higher Γ_r^{drift} term in the core region. Lastly, the both terms above mentioned would be increased by $\mathrm{E} \times \mathrm{B}$ drift by both the radial and perpendicular convection in both the core and SOL plasma. These cases are going to be figured out one by one in the next chapter.

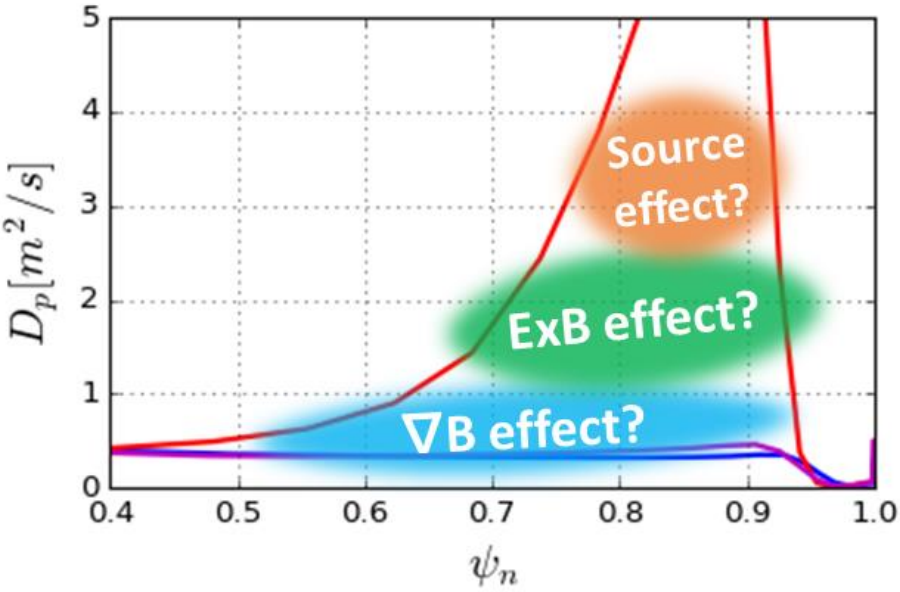

Figure 28. Particle diffusivities of each case of SN (blue), DN (red), and DN with SN plasma profiles (magenta). And possible reasons are colored.

3.2. Three Explanations of Density Pump-out in DN Transition

The proposed density pump-out reasons are investigated in this chapter. First, the ionization source rate is investigated with the modeled plasma profiles without drift effects. Then, the drift pattern will be studied first before evolving the plasma density converged with the effective diffusivities. The drift effects are estimated by the newly converged plasma profiles including some amount of the drift by solving the density equation in the fixed temperature.

3.2.1. Ionization Source

As shown in Figure 29, by comparing to DN configuration, the ionization source rate is dominant near the inner divertor of SN, which leads to the higher fueling to the edge pedestal density. Most of the ionization occurs near the X-points, including the inactive X-point of the SN configuration case. Unlike SN, the ionization in the PFR region is rather small in the DN case, and the ionization near the outer divertors is dominant. This degree of ionization source rate appeared to be related to the divertor heat flux.

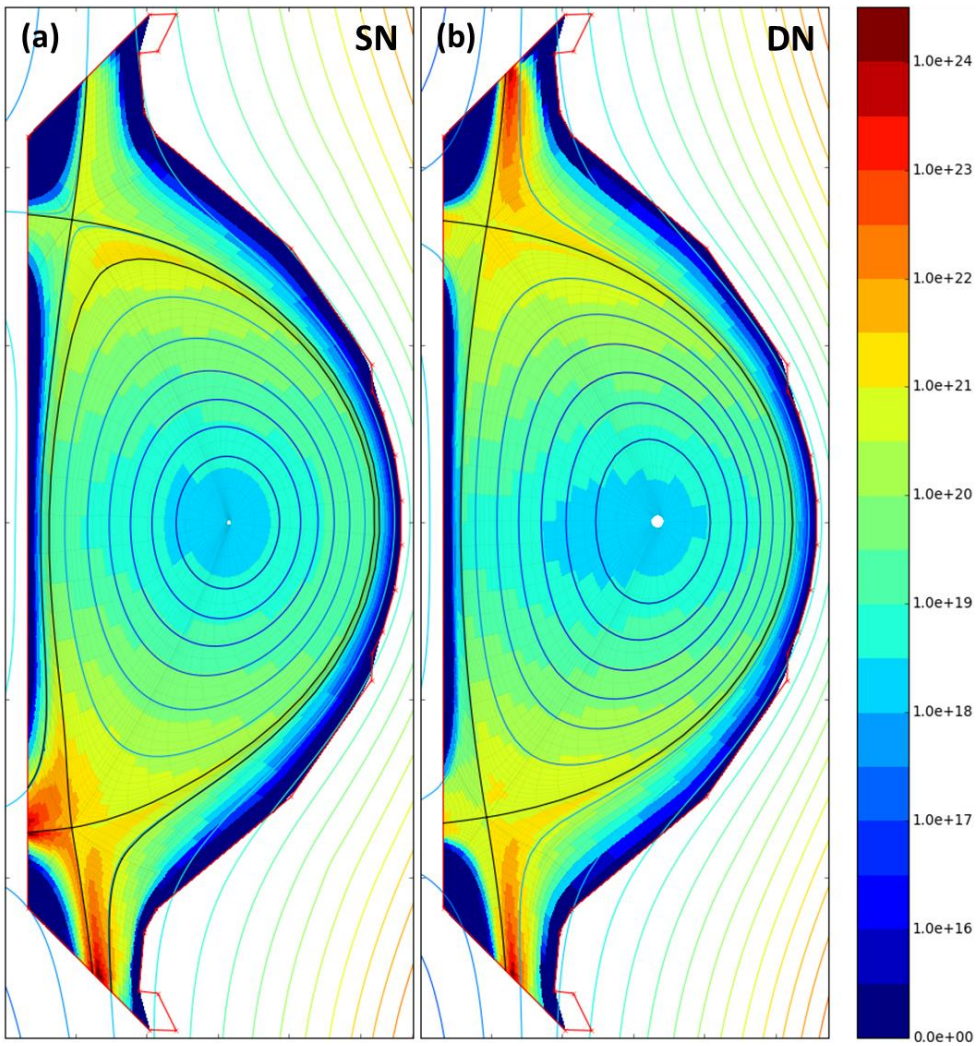

Figure 29. 2-D Mesh plot of the ionization source rate in SN (a) and DN (b) discharge.

In the other words, Figure 30 shows the divertor heat flux, heat flux that diverted normal to the divertor surface, at four strike points. In the SN, the divertor heat flux showed a larger peak and total amount in the inner divertor region than that of the outer, and no significant heat flux was observed in the two upper divertor without connection to the active SOL. In the case of DN, the magnitude of the heat flux

of the inner diverter was larger than expected. However, for the total amount, the outer divertors seem to be the main, which happened equally up and down. The difference between the two DN cases is noticed in the outer divertor region. The bump of the divertor heat flux of DN with SN profile case is higher. The higher density profiles may be the reason for inducing higher recycling at the outer divertor. The SN case has a similar divertor heat flux bump at both the inner and outer target.

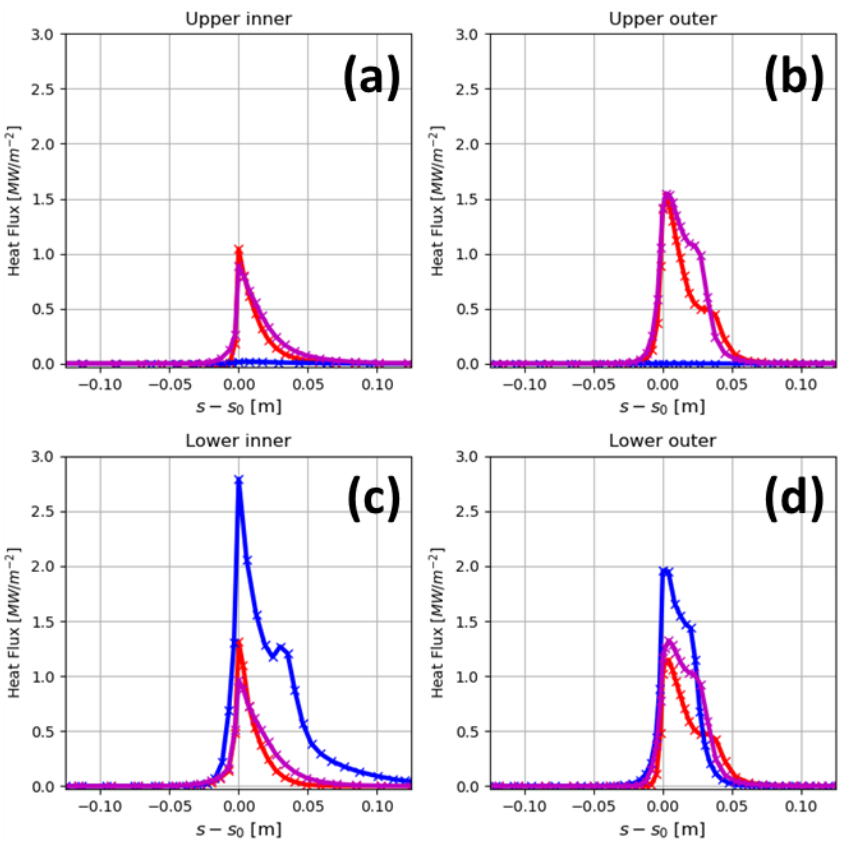

Figure 30. Divertor heat flux plot for each divertor with respect to the strike point. Blue for SN, red for DN, and magenta for DN using SN profiles. (a) Upper inner, (b) upper outer, (c) lower inner, and (d) lower outer divertor.

For a more detailed analysis, the poloidally surface averaged ionization source rate was calculated as shown in Figure 31. In the vicinity of the separatrix, the ionization rate was significantly higher in SN, but the effect decreased rapidly toward the core and became similar to or smaller than DN cases. It can be considered that it was difficult for neutral particles that had crossed the separatrix to penetrate into the core in the case of SN. For the DN configuration, there is two main neutral source region that makes the core plasma fuel twice during the particle transport poloidally.

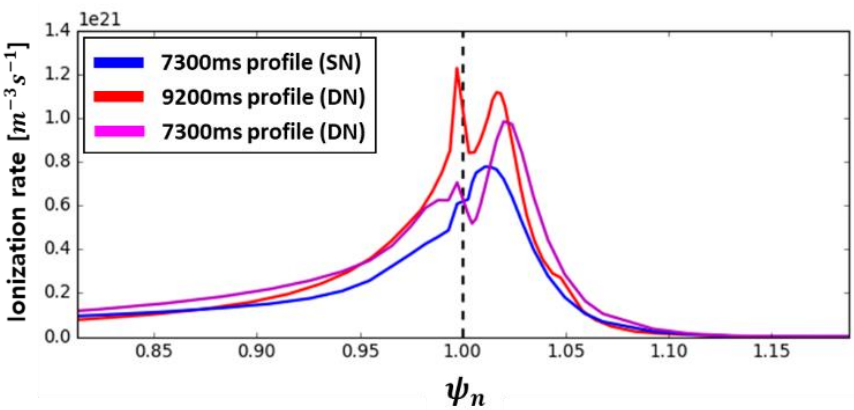

Figure 31. Surface averaged ionization source rate along the poloidal surface. Blue for SN, red for DN, and magenta for DN with SN profiles. The dotted line represents the separatrix.

Furthermore, the results when all ionization source rates occurring in the core plasma are summated, are shown in Figure 32.

When comparing the case of SN and the case of DN to which the SN plasma profile was applied, a clear difference in ionization source rate was not observed. As shown in Figure 32, in the case of SN, the ionization rate in HFS was higher than that in DN, but as the recycled neutral particle near the outer divertor in DN spread in the bulky LFS, larger in the plasma volume, the total sum produced a result roughly equivalent to that in the case of SN. The DN case clearly has less ionization source rate in the core plasma.

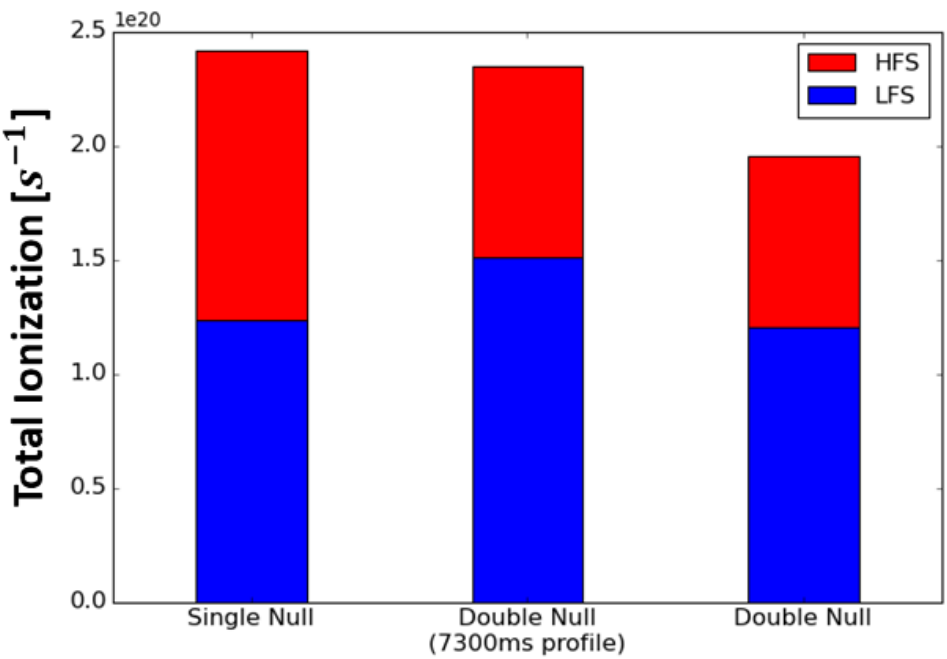

Figure 32. Total ionization rate in the core region. Blue for LFS, red for HFS. Left to Right; SN, DN with SN profile and DN.

As shown in the previous analysis of effective particle diffusivity, the difference in ionization sources according to the magnetic field

configurations is not significantly large when only the parallel velocity and anomalous radial diffusion are considered. In the first assumption presented in this paper, the difference in heat flux in the inner diverter was significant, but as the additional (formal inactive) X−point was attached to the core region, the outer divertors are connected, and the neutral particle transport was added from the outer divertor could not be ignored. This effect is expected to show a different aspect when E×B drift is introduced.

3.2.2. ∇B Drift Effect

∇B drift effects are investigated by using the two converged profiles above, which have the same profiles of SN to both SN and DN configurations. First, it is examined how ∇B drift flows in the reproduced plasma model. Then, the converged density profiles applying ∇B drift with fixed temperature profiles were compared by using an appropriate scaling factor.

(1) Difference of ∇B Drift direction in the HFS Core Plasma

Figure 33 is an arrow plot of ∇B drift flux calculated in the fixed converged plasma profiles. The direction of ∇B drift flux in HFS tends to be convex to the magnetic axis direction in the case of SN. This is not shown in the case of DN, but rather a vertical flow is observed. What can be inferred from this is that in the case of SN,

particles can be transported more inwardly in HFS. The ▽B drift fluxes in the SOL region have no significant differences between the configurations.

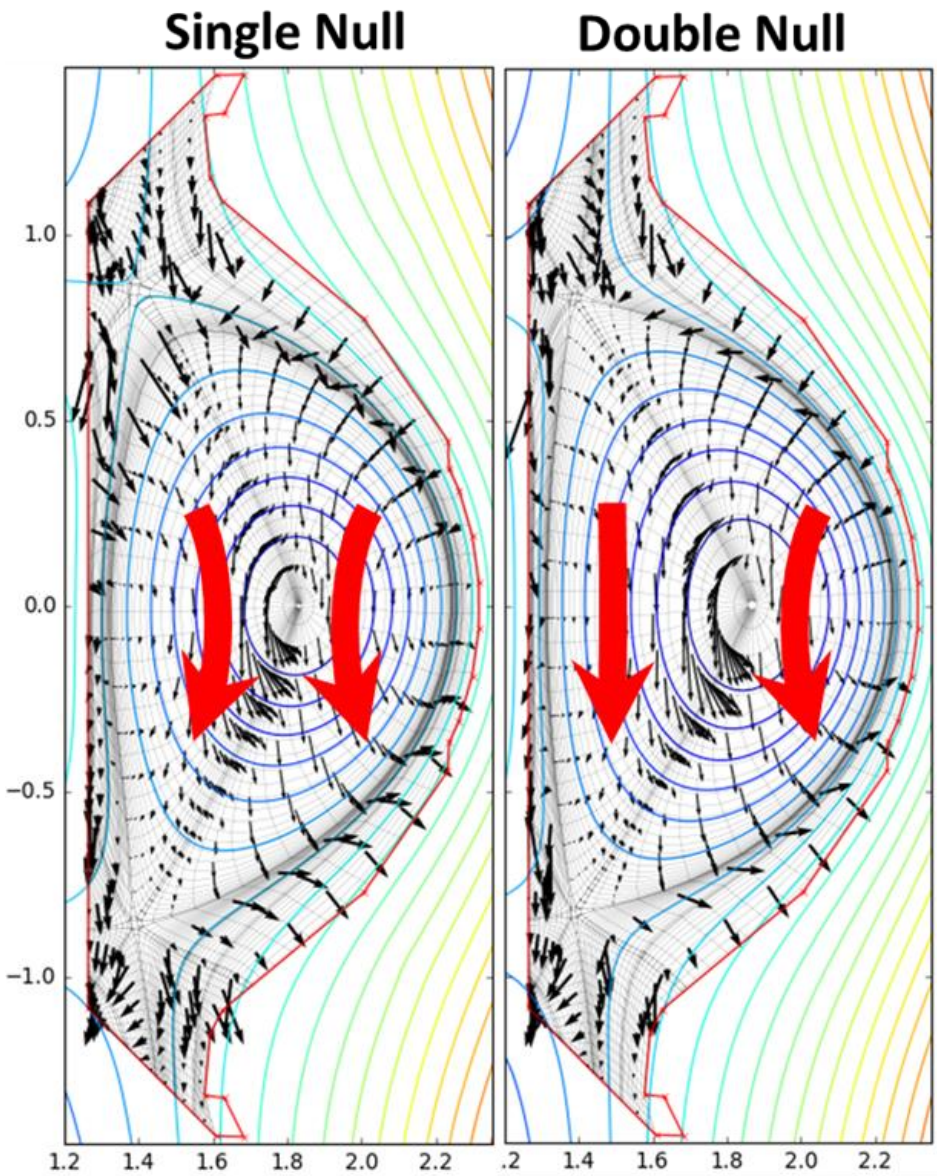

Figure 33. Arrow plots of the ▽B drift flux at the center of each cell. SN for left and DN for right.

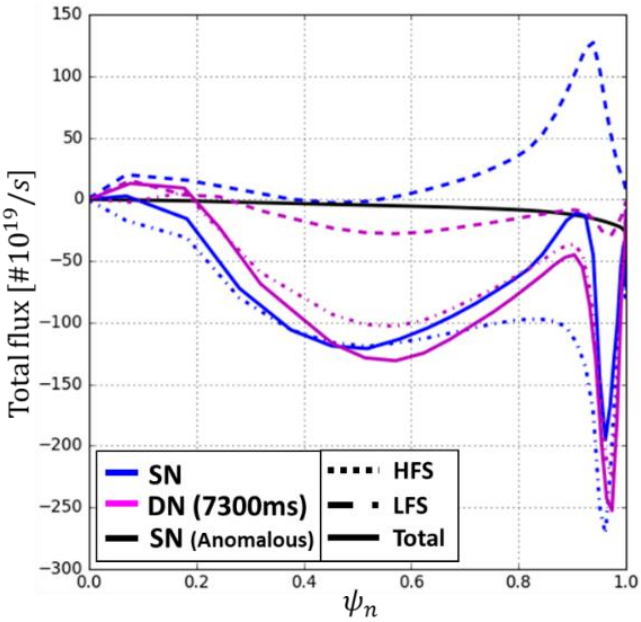

Figure 34. The surface sum of the total flux of each radial flux. Blue for ▽B drifts flux of SN, magenta for ▽B drift flux of DN with SN profiles, and black for the anomalous radial flux of SN. Dotted lines for the HFS surface, dot-dashed lines for the LFS surface, and solid lines for the total surface flux.

In order to examine the effect of this convex flow of SN, the total particle flux passing through each magnetic flux surface is calculated and presented in Figure 34. In the figure, HFS/LFS/Total represents the regions where the flux is summated. A positive value means the inward flux. In this result, the effective drift velocity is not applied due to it is needed to compare the original values of ▽B drift between the configurations. ▽B drift forms a comparable inward flux only in the HFS of SN, and in the case of DN, a small and outward flux can be calculated. Because of this, the total flow is slightly larger in the

case of DN. The flux quantities of the ▽B are enormous compared to the anomalous radial diffusion as shown in black. As mentioned in Chapter 2, this is a physically unsuitable result in the high-temperature range out of the fluid approach. Nevertheless, since the direction of the total flux at the relatively low-temperature edge pedestal is consistent, it can be seen that the difference due to drift between the two configurations occurs.

(2) Modeling the ion density with ∇B drift

In order to examine the effect of these flux directions on the change in plasma density, ▽B drift is applied to the SN and the DN plasma, which had previously converged with the effective diffusivities, respectively. At this time, it was decided to apply a value smaller than the actual calculated ▽B drift value by using a scaling factor. Because the assumption for calculating the effective diffusivity is that this diffusion flux effectively models most of the phenomena of the plasma profile, if the drift effect is considered too large, the results must be highly duplicated. Also, as shown in Figure 34, we already mentioned that the flux due to ▽B drift is much larger than the total amount of radial diffusion calculated by effective diffusivity, so it is very difficult to secure numerical stability even though the applied effective drift velocity regulates up to the thermal velocity. The factor applied to the following simulation, $\mathrm{f}_{\mathrm{scaling}}^{\nabla B} = 0.2$, was examined

for each SN and DN.

The calculated 2-D density profiles are presented in Figure 35. It is clear that the core plasma density pump-out to the different divertor through the SOL region: lower inner and outer divertor for SN, and upper and lower outer divertor for DN. The HFS SOL in DN clearly separated from the LFS in this ∇B drift modeling. A hint of the vertical flow is shown at the upper PFR.

Figure 36 shows the results of the density profiles of SN and DN at the Outer Mid-Plane (OMP). In both profiles, a lot of convection occurred in the core and was transported into the SOL plasma. Because the larger flux than the parallel convection in the SOL plasma flows down to the SOL region, the SN has a higher density at the SOL than the core. This could also be a problem seen as a result of not adjusting the gas pump. However, what we should pay attention to here is that the convection difference in density can occur only with the difference in magnetic field configuration due to ∇B drift. This difference affects the overall core plasma, but the shape of the profile seems to be maintained. In short, the effect of ∇B drift can induce a density decrease due to the convection of the core plasma, and the effect can be said to be greater in DN than in SN.

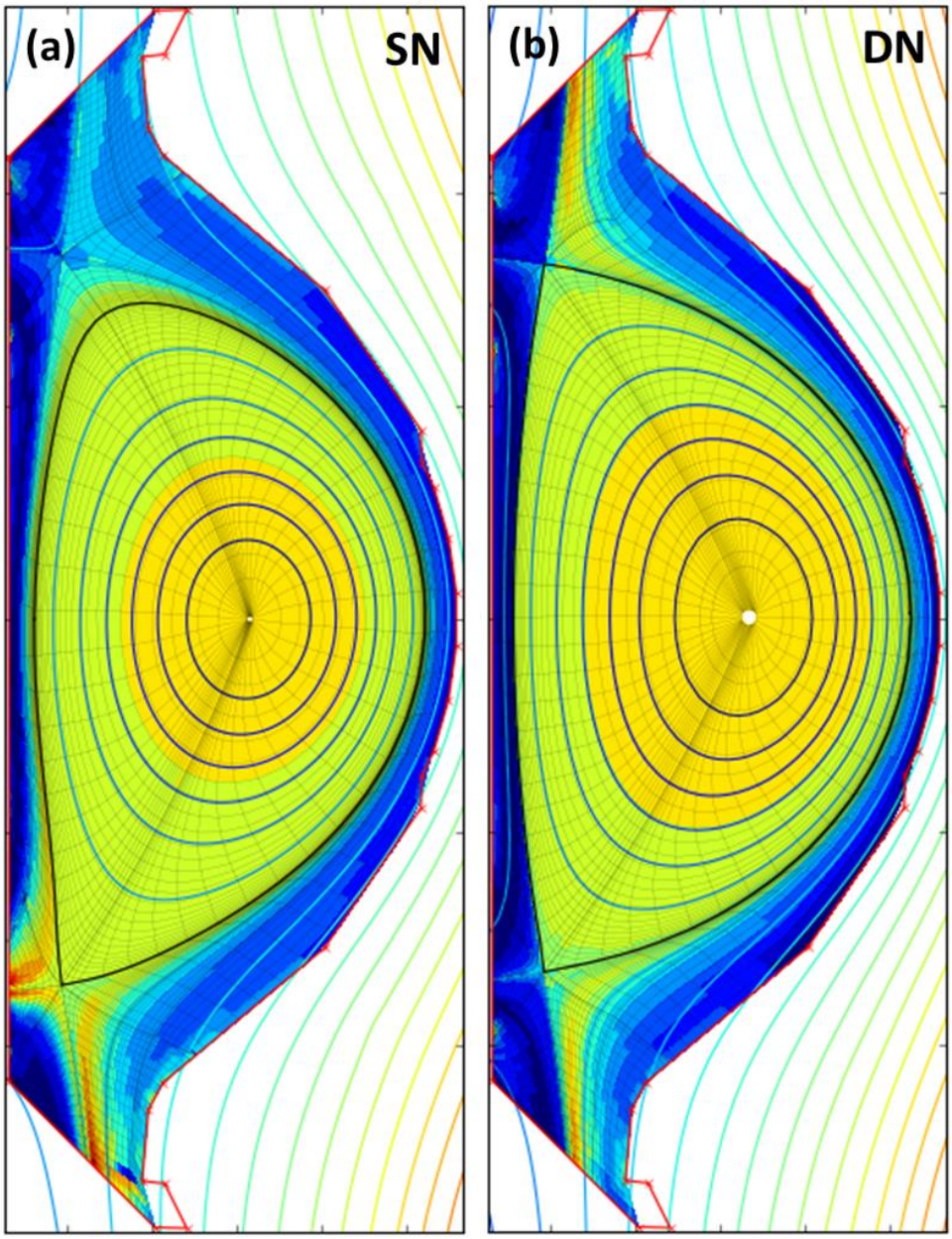

Figure 35. 2-D mesh plot of the density profiles after ▽B drift was applied. (a) for SN, and (b) for DN configurations.

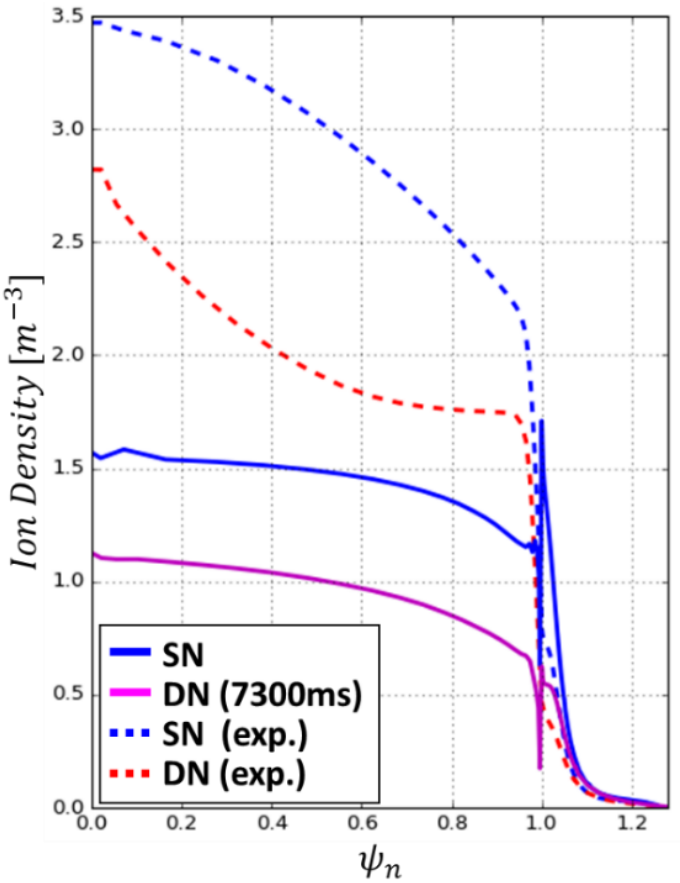

Figure 36. Ion density with respect to the normalized psi when ▽B is applied. The blue solid line is the SN result, the red solid line for DN with SN profiles, and the dotted line represent the experiment fitting profiles of SN and DN.

3.2.3. E×B Drift Effect

The previous research procedure is also applied to the E×B drift case. However, in this case, not only the drift flux in the core plasma but also the flow in the SOL is important. Therefore, the ionization source rate is presented and analyzed, first.

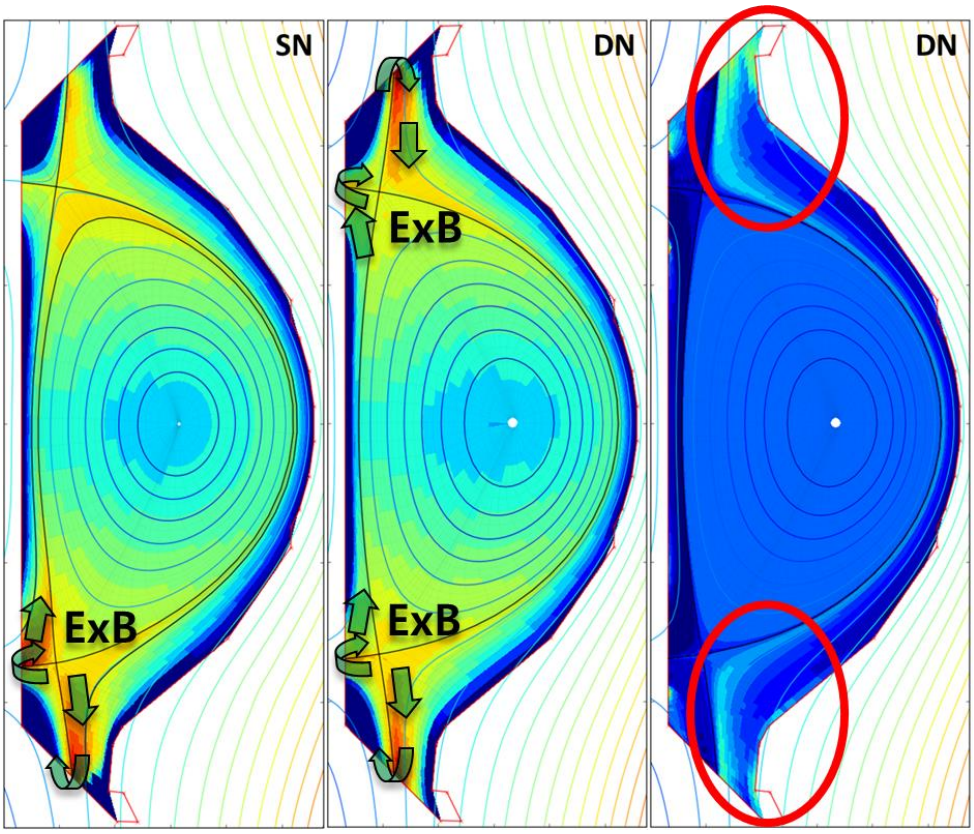

Figure 37. 2-D mesh plot of ionization source rate for SN and DN, and recombination sink rate for DN. The green arrows indicate the ExB flux near the divertor.

(1) E×B drift driven ionization source rate

E×B drift has changed the existing flow very much, especially in the SOL region. Figure 37 shows the ionization source rate and recombination sink rate for each magnetic field configuration along with the E×B drift flow direction. As expected in 1.2.3., the ionization source rate due to E×B drift moved to the inner divertor side by the

plasma flux flowing inward from the outer near the lower divertor area (favorable side). This effect produces the result of further increasing the recycling contribution of the lower inner divertor, which was already dominant in SN, and this appears also in DN. In the upper divertor area, the opposite phenomenon occurs, the particle flux flows from inner to outer under the E×B drift effect. Due to the newly introduced particle flux, the ionization source rate is higher in the upper part of the DN plasma, resulting in up-and-down asymmetry.

This difference in flow can also be confirmed in the recombination sink rate. Recombination of Deuterium occurs only at relatively low temperatures and is concentrated in the SOL region. In addition, due to the effect of E×B drift, an up-and-down asymmetry is confirmed even though the previous symmetric temperature profiles are used.

This trend can also be seen in the divertor heat flux as shown in Figure 38. In both SN and DN cases, it can be seen that the inner divertor heat flux increased and relatively decreased in the outer near the favorable side. On contrary, in the case of DN, the upper side outer divertor heat flux increased. Also, the increased flow due to E×B drift caused the calculated divertor heat flux level at SN to be abnormally high (higher than 20 MW/m^3, which is a conventional engineering limit for the divertor material). Therefore, in the case of SN, the recycling near the inner divertor side increases significantly compared to the previous results, making the pedestal density very high. On the other hand, it can be expected that the change in the DN

case will not be significant.

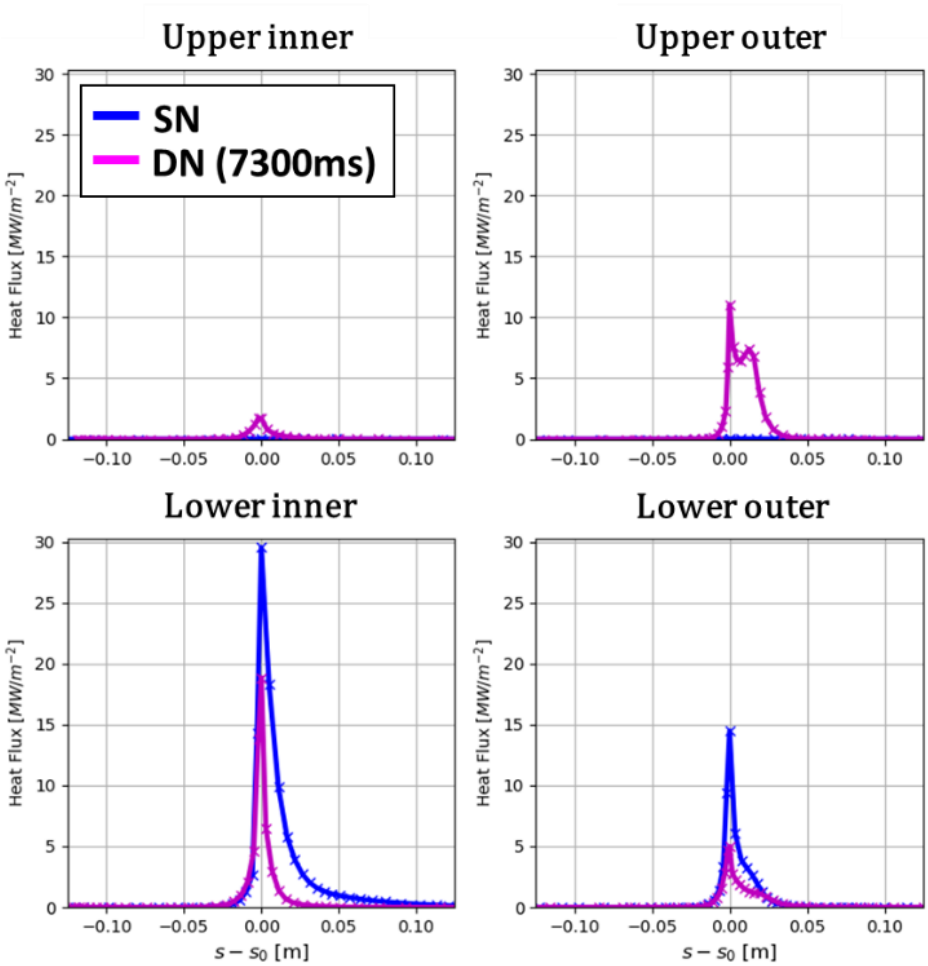

Figure 38. Divertor heat fluxes of SN (blue) and DN (magenta) for each divertor.

(2) Particle source effect by E×B drift near the edge pedestal

As in the previous case, the temperature is fixed and the converged density profile results using $f_{\text{scaling}}^{ExB} = 0.2$ are shown in Figure 39. The two-dimensional density fluctuation is shown in the core plasma of

both SN and DN cases. By comparing these results to that in Figure 35, it is clear that the E×B drift transports the particles to the HFS SOL region even in the DN configuration. By the way, some data that seem to have numerical errors are shown at the edge of the outer divertor due to the fast parallel velocity flow where very low-density profiles are placed.

In Figure 40, the 1-D density profiles are shown. Similar to the case of ▽B drift, it can be confirmed that the SOL parallel flow does not sufficiently transport the additional particle flux introduced from the core plasma and the SOL has a very large decaying length. And a very large oscillation can be observed near the edge pedestal region. This is because the E×B drift flow shear made from the gradient of the electrostatic potential formed near the X-point creates a spiral-shaped density fluctuation in the edge pedestal area as shown in Figure 41. This shape was not visible unless ExB drift was applied, and even if the temperature was solved, the temperature profile was almost poloidally even, so it had no effect. Therefore, this is a part that requires accuracy or physical analysis of the model used, which will be discussed later.

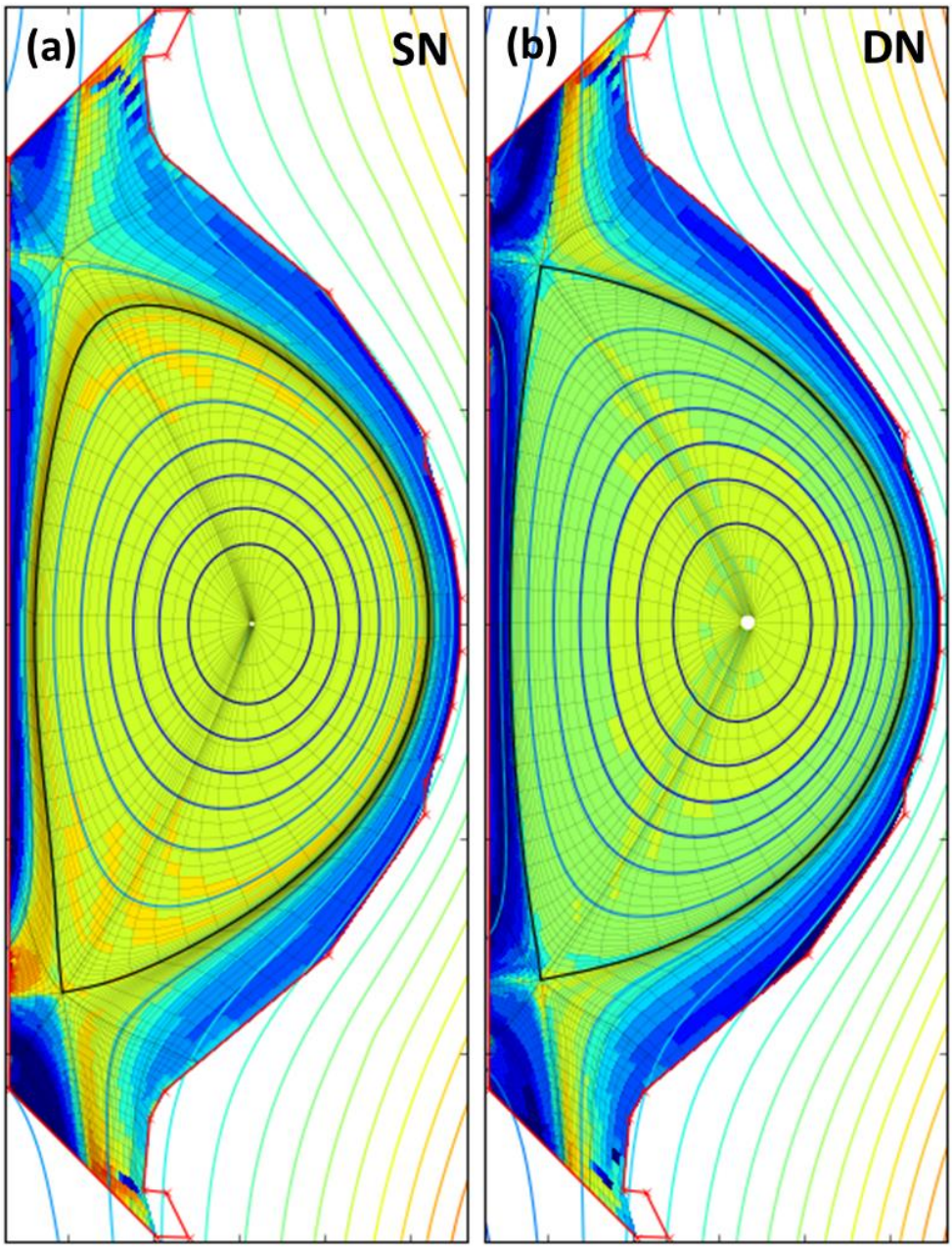

Figure 39. 2-D mesh plot of the density profiles after E × B drift applied. (a) for SN, (b) for DN configurations.

Nevertheless, two effects can be observed through the converged

profile. The first is that the core plasma can gradually decrease by E×B drift convection in both SN and DN. This is interpreted as the $E_{\perp} \times B$ drift occurring in the core due to the aforementioned density fluctuation of the spiral structure to form a radial flow. The difference in the effect between SN and DN, judging by the core value near the magnetic axis, may not be very large.

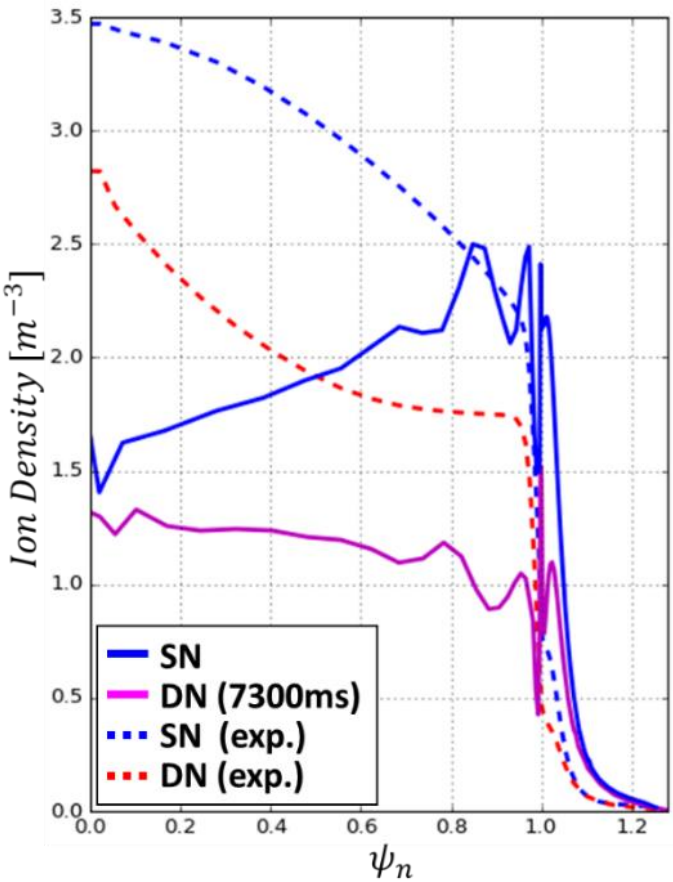

Figure 40. Ion density with respect to the normalized psi when $\mathbf{E} \times \mathbf{B}$ drift applied

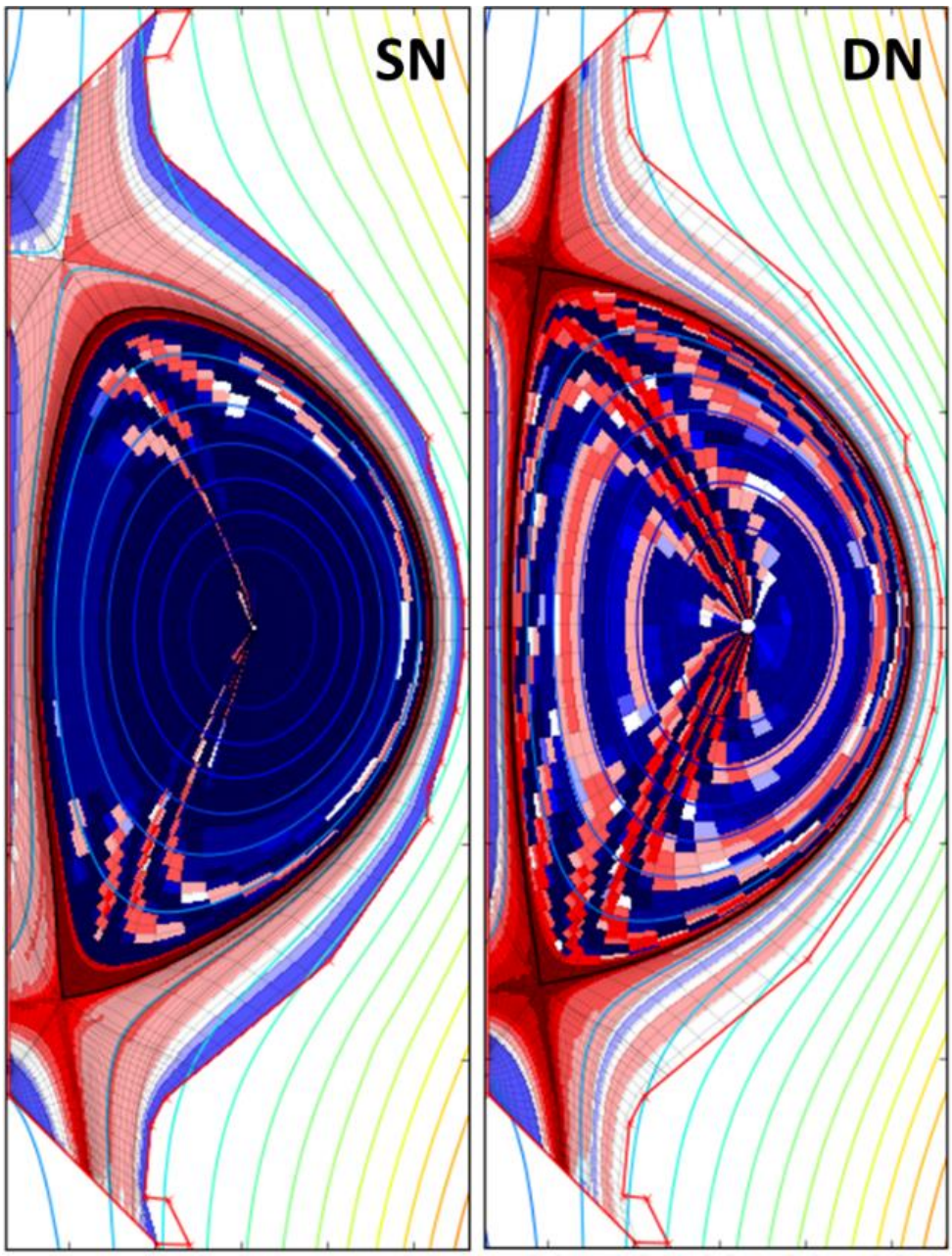

Figure 41. 2-D mesh plot of electrostatic potential in SN and DN configurations.

Second, the difference in the particle fueling in the pedestal area can

be confirmed. In the case of SN, a lot of plasma is transported from the core, but the height of the pedestal was maintained by the particle fueling from the SOL region, especially from the inner divertor. But, it was not the case in DN. Although the density of HFS SOL increased compared to the ∇B drift case, it can be expected that the recycling effect will be very small, and most of the flux will flow to the outer diverter. Certainly, the $E \times B$ drift flux flowing near the additional X-point seems to have the effect of reducing the source of the density profile.

Chapter 4.
Conclusion and Future Work

4.1. Conclusion

In this dissertation, the KSTAR DN transition discharge is modeled by a developed 2-D plasma modeling system and analyzed by the three reasons why the core plasma density is pumped out during the DN transition from the SN configuration. The converged plasma profiles of SN and DN configuration, which are only applied to the parallel velocity and the anomalous radial diffusion, shows little difference in the ionization source rate between the configurations. However, like a perturbative analysis, when some portion of the ∇B or $E \times B$ drift is applied to the converged plasma the density decreased differently with respect to the magnetic field configuration. In the ∇B case, the direction of the drift convection is different, only the SN configuration has the inward flux at the HFS, which leads to

pumping out the density in the DN configuration more by the ∇B drift.

On the other hand, $E \times B$ drift affects the plasma density in two ways. The one is that the $E \times B$ drift induces the particle flux to flow to the inner divertor from the outer adjacent to the favorable X-point. Then, the recycling near the inner divertor is accelerated leading to increasing the edge pedestal density fueling. But, if there are two X-points in the core, this particle fueling is canceled out by the opposite flux near the unfavorable X-point. The oppositely directed flux to the outer divertor pumps out the edge pedestal and SOL density to the gas outlet.

The second is that the $E \times B$ drift makes outward convections in the core region by the two-dimensional density fluctuation at the edge region. We speculated this density fluctuation originated from the electrostatic potential gradient near the X-points. Without the drift, the potential is almost evenly distributed in the diamagnetic direction except near the X-points. This gradient may make a seed radial $E_{\perp} \times B$ drift becoming the spiral density fluctuation. This kind of fluctuation is usually seen in turbulent simulations with the electric field or effect of the X-points [76], [77]. Therefore, it might be one of the turbulence mode-like phenomena near the pedestal.

Or, this fluctuation survived near the edge region where the parallel velocity turns over its direction due to the toroidal rotation is not considered in this modeling. This means that the fluctuation might come from the mis-consideration or the numerical oscillation. So, a detailed analysis is needed and the plan will be stated in future

work.

Unlike the results of this study, according to the simulation conducted internally, it was confirmed that the fast ion content increased by NBI when the density decreased, but the temperature did not rise as in the experiment. This seems to have offset the rise caused by the additional heating due to the convective effect of the newly applied drift, especially in the case of ions, the temperature has dropped. It is judged that the effect of this drift is greater due to the convective effect from the ▽B drift than in the case of E×B. Therefore, attention is paid to the Pfirsh-Schlüter current derived from the charge separation caused by this ▽B drift.

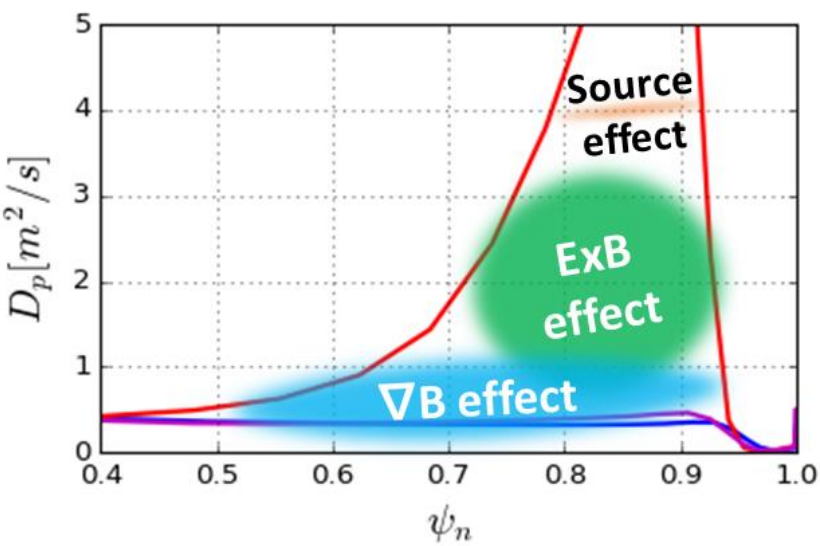

Figure 42. Particle diffusivities of each case of SN (blue), DN (red), and DN with SN plasma profiles (magenta). And reasons for the deviation are colored by their expected contribution.

In addition, as the plasma changes, this study proceeds without calculating the transport model, so it is expected that the response of the actual plasma converges quite differently. Therefore, more predictive modeling should be attempted, such as employing a neoclassical model and a turbulence model. In addition, it is also necessary to consider how to handle the particle/heat flux escaping from the magnetic flux surface, that these models usually provide, to distribute on the poloidal plane.

Besides, the developed 2-D plasma modeling system already shows the potential to figure out the two-dimensional phenomena that occur throughout the entire tokamak chamber. Although this system is able to model the D only, it can be used to analyze the 2-D core-edge-SOL-wall plasma simultaneously, making it easy to obtain a general understanding. In addition, it has the advantage of being able to conduct various case studies with a relatively fast calculation speed.

4.2. Future Work

Although this dissertation was able to discover these new facts, it also highlighted many unresolved problems and requirements. First, an analysis of one discharge was performed using the developed code, but modeling of several other DN transition discharges was not performed. Among these discharges, there are experiments in which density pump-out does not occur even during the DN transition, and the reasons presented in this study may not explain this. In addition, the experiment in this paper was a discharge in transition from favorable LSN to DN, and it is necessary to study whether this phenomenon also occurs in unfavorable USN to DN transition.

Furthermore, the temperature was fixed in this research, so, we mentioned the Pfirsh-Schlüter current which might compensate for the temperature decreased by the ∇B drift-driven convection. Besides, this current will change the potential also, so the $E \times B$ drift should be calculated differently. The detailed effects should be discussed later. In addition, in this study, the impurity is out of consideration (using $Z_{eff} = 2.0$), and these impurities are expected to be pumped out together with the ion. So, if considering their transport, it is expected that the temperature will rise.

Finally, for the developed system, numerical/practical issues need to be improved. For example, the convergence of the potential solution must be checked to use the $E \times B$ drift. It includes the

simulation timescale, the grid size dependency, the discretization method, and the model self-consistency with other plasma equations. On the other hand, in the case of a grid applied from the SOL to the wall, there is a misalignment in the direction of the magnetic field, resulting in dependency in the grid shape. Therefore, it is necessary to complete a system that flexibly solves according to the direction of the magnetic field in the cell shape. Also, when dealing with quasi-orthogonal meshes, the cross-diffusion term should be considered. Lastly, the current calculation speed should be further improved so that simulations for more diverse cases can be performed.

Bibliography

[1] "National Ignition Facility achieves fusion ignition | Lawrence Livermore National Laboratory." https://www.llnl.gov/news/national-ignition-facility-achieves-fusion-ignition (accessed Jan. 10, 2023).

[2] "What is Fusion, and Why Is It So Difficult to Achieve? | IAEA." https://www.iaea.org/bulletin/what-is-fusion-and-why-is-it-so-difficult-to-achieve (accessed Jan. 10, 2023).

[3] "The bizarre reactor that might save nuclear fusion | Science | AAAS." https://www.science.org/content/article/bizarre-reactor-might-save-nuclear-fusion (accessed Jan. 10, 2023).

[4] K. Riße, "Experiences from design and production of wendelstein 7-X magnets," *Fusion Engng Des*, vol. 84, no. 7–11, pp. 1619–1622, Jun. 2009, doi: 10.1016/j.fusengdes.2009.01.064.

[5] A. Dinklage *et al.*, "Magnetic configuration effects on the Wendelstein 7-X stellarator," *Nature Physics 2018 14:8*, vol. 14, no. 8, pp. 855–860, May 2018, doi: 10.1038/s41567-018-0141-9.

[6] H. Meyer *et al.*, "H-mode physics of near double null plasmas in MAST and its applications to other tokamaks," *Nuclear Fusion*, vol. 46, no. 1, p. 64, Dec. 2005, doi: 10.1088/0029-5515/46/1/008.

[7] H. H. Lee *et al.*, "Thermographic studies of outer target heat fluxes on KSTAR," *Nuclear Materials and Energy*, vol. 12, pp. 541–547, Aug. 2017, doi: 10.1016/J.NME.2016.12.019.

[8] T. W. Petrie *et al.*, "Changes in edge and scrape-off layer plasma behavior due to variation in magnetic balance in DIII-D," *Journal of Nuclear Materials*, vol. 313–316, no. SUPPL., pp. 834–838, Mar. 2003, doi: 10.1016/S0022-3115(02)01459-9.

[9] T. W. Petrie *et al.*, "Comparison of radiating divertor behaviour in single-null and double-null plasmas in DIII-D," *Nuclear Fusion*, vol. 48, no. 4, p. 045010, Mar. 2008, doi: 10.1088/0029-5515/48/4/045010.

[10] D. Brunner, A. Q. Kuang, B. Labombard, and J. L. Terry, "The dependence of divertor power sharing on magnetic flux balance in near double-null configurations on Alcator C-Mod," *Nuclear Fusion*, vol. 58, no. 7, p. 076010, May 2018, doi: 10.1088/1741-4326/AAC006.

[11] N. Smick, B. Labombard, and I. H. Hutchinson, "Transport and drift-driven plasma flow components in the Alcator C-Mod boundary plasma," *Nuclear Fusion*, vol. 53, no. 2, Feb. 2013, doi: 10.1088/0029-5515/53/2/023001.

[12] G. M. Wallace *et al.*, "Heating and current drive actuators study for FNSF in the ion cyclotron and lower hybrid range of frequency," *Fusion Engineering and Design*, vol. 135, pp. 370–379, Oct. 2018, doi: 10.1016/J.FUSENGDES.2017.06.025.

[13] G. L. Kulcinski and R. W. Conn, *Conceptual design of a 5000 MW(th) D-T Tokamak reactor*. International Atomic Energy Agency (IAEA): IAEA, 1974. [Online]. Available: http://inis.iaea.org/search/search.aspx?orig_q=RN:06211457

[14] D. Post *et al.*, "Physics aspects of the compact ignition tokamak," *Phys Scr*, vol. 1987, no. T16, pp. 89–106, Jan. 1987, doi: 10.1088/0031-8949/1987/T16/011.

[15] D. E. Post, "ITER: Physics basis," *IEEE Conference Record - Abstracts*, p. 109, 1990, doi: 10.1109/PLASMA.1990.110570.

[16] F. Najmabadi *et al.*, "The ARIES-I Tokamak Reactor Study†," *Fusion Technology*, vol. 19, no. 3P2A, pp. 783–790, May 1991, doi: 10.13182/FST91-A29440.

[17] F. Najmabadi *et al.*, "Spherical torus concept as power plants—the ARIES-ST study," *Fusion Engineering and Design*, vol. 65, no. 2, pp. 143–164, Feb. 2003, doi: 10.1016/S0920-3796(02)00302-2.

[18] C. E. Kessel *et al.*, "The ARIES Advanced and Conservative Tokamak Power Plant Study," *Fusion Science and Technology*, vol. 67, no. 1, pp. 1–21, Jan. 2015, doi: 10.13182/FST14-794.

[19] G. H. Neilson, "II. Device Description and General Physics Requirements," *Fusion Technology*, vol. 21, no. 3P1, pp. 1056–1075, May 1992, doi: 10.13182/FST92-A29892.

[20] D. M. Meade, "FIRE, a next step option for magnetic fusion," *Fusion Engineering and Design*, vol. 63–64, pp. 531–540, Dec. 2002, doi: 10.1016/S0920-3796(02)00282-X.

[21] S. Kwon *et al.*, "Recent progress in the design of the K-DEMO divertor," *Fusion Engineering and Design*, vol. 159, p. 111770, Oct. 2020, doi: 10.1016/J.FUSENGDES.2020.111770.

[22] B. N. Sorbom *et al.*, "ARC: A compact, high-field, fusion nuclear science facility and demonstration power plant with demountable magnets," *Fusion Engineering and Design*, vol. 100, pp. 378–405, Nov. 2015, doi: 10.1016/J.FUSENGDES.2015.07.008.

[23] G. S. Lee *et al.*, "Design and construction of the KSTAR tokamak," *Nuclear Fusion*, vol. 41, no. 10, p. 1515, Oct. 2001, doi: 10.1088/0029-5515/41/10/318.

[24] H. K. Park *et al.*, "Overview of KSTAR research progress and future plans toward ITER and K-DEMO," *Nuclear Fusion*, vol. 59, no. 11, p. 112020, Jul. 2019, doi: 10.1088/1741-4326/AB20E2.

[25] Y. K. Oh *et al.*, “Progress of the KSTAR Research Program Exploring the Advanced High Performance and Steady-State Plasma Operations,” *Journal of the Korean Physical Society*, vol. 73, no. 6, pp. 712–735, Sep. 2018, doi: 10.3938/JKPS.73.712/METRICS.

[26] Y. S. Na *et al.*, “On hybrid scenarios in KSTAR,” *Nuclear Fusion*, vol. 60, no. 8, Aug. 2020, doi: 10.1088/1741-4326/ab8b7a.

[27] H. Han *et al.*, “A sustained high-temperature fusion plasma regime facilitated by fast ions,” *Nature 2022 609:7926*, vol. 609, no. 7926, pp. 269–275, Sep. 2022, doi: 10.1038/s41586-022-05008-1.

[28] G. Park *et al.*, “Overview of recent progress in 3D field physics in KSTAR,” *Journal of the Korean Physical Society 2022 80:8*, vol. 80, no. 8, pp. 759–786, Feb. 2022, doi: 10.1007/S40042-022-00423-Z.

[29] J. K. Park *et al.*, “3D field phase-space control in tokamak plasmas,” *Nature Physics 2018 14:12*, vol. 14, no. 12, pp. 1223–1228, Sep. 2018, doi: 10.1038/s41567-018-0268-8.

[30] J. G. Kwak *et al.*, “KSTAR Status and Upgrade Plan Toward Fusion Reactor,” *IEEE Transactions on Plasma Science*, vol. 48, no. 6, pp. 1388–1395, Jun. 2020, doi: 10.1109/TPS.2020.2964776.

[31] S. G. Lee *et al.*, “Overview and recent progress of KSTAR diagnostics,” *Journal of Instrumentation*, vol. 17, no. 01, p. C01065, Jan. 2022, doi: 10.1088/1748-0221/17/01/C01065.

[32] G. R. McKee, R. J. Fonck, M. W. Shafer, I. U. Uzun-Kaymak, and Z. Yan, “Wide-field turbulence imaging with beam emission spectroscopy,” *Review of Scientific Instruments*, vol. 81, no. 10, p. 10D741, Oct. 2010, doi: 10.1063/1.3495788/1.3495788.MM.ORIGINAL.V1.MOV.

[33] S.-H. Hong *et al.*, “Plasma-Surface Interaction Activities in KSTAR,” *Fusion Science and Technology*, vol. 63, no. 1T, pp. 88–93, May 2013, doi: 10.13182/FST13-A16879.

[34] K. C. Lee *et al.*, “The design of two color interferometer system for the 3-dimensional analysis of plasma density evolution on KSTAR,” *Fusion Engineering and Design*, vol. 113, pp. 87–91, Dec. 2016, doi: 10.1016/J.FUSENGDES.2016.10.008.

[35] J. W. Juhn *et al.*, “Multi-chord IR-visible two-color interferometer on KSTAR,” *Rev Sci Instrum*, vol. 92, no. 4, Apr. 2021, doi: 10.1063/5.0043811.

[36] J. H. Lee, S. T. Oh, and H. M. Wi, “Development of KSTAR Thomson scattering systema),” *Review of Scientific Instruments*, vol. 81, no. 10, p. 10D528, Oct. 2010, doi: 10.1063/1.3494275.

[37] W. H. Ko, S. Oh, and M. Kwon, “KSTAR charge exchange spectroscopy system,” *IEEE Transactions on Plasma Science*, vol. 38, no. 4 PART 4, pp. 996–1000, Apr. 2010, doi: 10.1109/TPS.2010.2042182.

[38] 이영호, “Effect of coherent edge mode on high-performance transition in KSTAR hybrid scenario discharges,” 2022.

[39] H. R. Wilson *et al.*, “Ideal magnetohydrodynamic stability of the tokamak high-confinement-mode edge region,” *Phys Plasmas*, vol. 6, no. 5, p. 1925, Apr. 1999, doi: 10.1063/1.873492.

[40] H. Arnichand *et al.*, “Quasi-coherent modes and electron-driven turbulence,” *Nuclear Fusion*, vol. 54, no. 12, p. 123017, Nov. 2014, doi: 10.1088/0029-5515/54/12/123017.

[41] T. Zhang *et al.*, “Outward particle transport by coherent mode in the H-mode pedestal in the Experimental Advanced Superconducting Tokamak (EAST),” *Plasma Phys Control Fusion*, vol. 59, no. 6, May 2017, doi: 10.1088/1361-6587/aa69e8.

[42] Youngho Lee *et al.*, “Effect of coherent edge-localized mode on transition to high-performance hybrid scenarios in KSTAR,” *Nuclear Fusion (submitted)*, 2023.

[43] W. Lee, J. Lee, D. J. Lee, H. K. Park, and Kstar Team, “Study of the origin of quasi-coherent modes in low-density KSTAR ECH plasmas,” *Nuclear Fusion*, vol. 61, no. 1, p. 016008, Nov. 2020, doi: 10.1088/1741-4326/ABBDC0.

[44] K. H. Burrell *et al.*, “Advances in understanding quiescent H-mode plasmas in DIII-Da),” *Phys Plasmas*, vol. 12, no. 5, p. 056121, Apr. 2005, doi: 10.1063/1.1894745.

[45] A. A. Vlasov, “The vibrational properties of an electron gas,” *Uspekhi Fizicheskih Nauk*, vol. 93, no. 11, pp. 444–470, Nov. 1967, doi: 10.3367/UFNR.0093.196711F.0444.

[46] J. M. Park *et al.*, “Integrated modeling of core, edge pedestal and scrape-off-layer for high β N steady-state scenarios on DIII-D,” in *2018 IAEA Fusion Energy Conf.*, 2018, p. TH-P7.

[47] M. Romanelli *et al.*, “JINTRAC: A System of Codes for Integrated Simulation of Tokamak Scenarios,” *Plasma and Fusion Research*, vol. 9, no. SPECIALISSUE.2, pp. 3403023–3403023, Apr. 2014, doi: 10.1585/PFR.9.3403023.

[48] R. Zagórski, G. Telesca, and J. Rappj, “Integrated modelling of nitrogen seeded JET discharges,” *Contributions to Plasma Physics*, vol. 48, no. 1–3, pp. 179–184, Mar. 2008, doi: 10.1002/CTPP.200810032.

[49] C. Y. Lee *et al.*, “Development of integrated suite of codes and its validation on KSTAR,” *Nuclear Fusion*, vol. 61, no. 9, Sep. 2021, doi: 10.1088/1741-4326/ac1690.

[50] O. Meneghini and L. Lao, “Integrated Modeling of Tokamak Experiments with OMFIT,” *Plasma and Fusion Research*, vol. 8, no. SPL.ISS.1, pp. 2403009–2403009, Apr. 2013, doi:

10.1585/PFR.8.2403009.

[51] W. R. Elwasif *et al.*, "The design and implementation of the SWIM integrated plasma simulator," *Proceedings of the 18th Euromicro Conference on Parallel, Distributed and Network-Based Processing, PDP 2010*, pp. 419–427, 2010, doi: 10.1109/PDP.2010.63.

[52] V. Basiuk *et al.*, "Simulations of steady-state scenarios for Tore Supra using the CRONOS code," 2003. [Online]. Available: http://iopscience.iop.org/0029-5515/43/9/305

[53] S. Wiesen *et al.*, "On the role of finite grid extent in SOLPS-ITER edge plasma simulations for JET H-mode discharges with metallic wall," *Nuclear Materials and Energy*, vol. 17, pp. 174–181, Dec. 2018, doi: 10.1016/J.NME.2018.10.013.

[54] D. Reiter, M. Baelmans, and P. Börner, "The EIRENE and B2-EIRENE Codes," *https://doi.org/10.13182/FST47-172*, vol. 47, no. 2, pp. 172–186, 2017, doi: 10.13182/FST47-172.

[55] W. Dekeyser *et al.*, "Plasma edge simulations including realistic wall geometry with SOLPS-ITER," *Nuclear Materials and Energy*, vol. 27, p. 100999, Jun. 2021, doi: 10.1016/J.NME.2021.100999.

[56] C. F. Sang, H. Y. Guo, P. C. Stangeby, H. Q. Wang, L. Wang, and D. Z. Wang, "SOLPS analysis of changes in the main SOL of DIII-D associated with divertor detachment vs attachment and closure vs openness," *Nuclear Fusion*, vol. 60, no. 5, p. 056011, Apr. 2020, doi: 10.1088/1741-4326/AB7C29.

[57] H. Lütjens, A. Bondeson, and O. Sauter, "The CHEASE code for toroidal MHD," 1996.

[58] "FreeGS: Free boundary Grad-Shafranov solver," *https://github.com/bendudson/freegs.*

[59] A. Pankin, D. McCune, R. Andre, G. Bateman, and A. Kritz, "The tokamak Monte Carlo fast ion module NUBEAM in the National Transport Code Collaboration library," *Comput Phys Commun*, vol. 159, no. 3, pp. 157–184, Jun. 2004, doi: 10.1016/J.CPC.2003.11.002.

[60] G. M. Staebler, J. E. Kinsey, and R. E. Waltz, "A theory-based transport model with comprehensive physicsa)," *Phys Plasmas*, vol. 14, no. 5, p. 055909, May 2007, doi: 10.1063/1.2436852.

[61] R. E. Waltz, G. M. Staebler, W. Dorland, G. W. Hammett, M. Kotschenreuther, and J. A. Konings, "A gyro-Landau-fluid transport model," *Phys Plasmas*, vol. 4, no. 7, p. 2482, Sep. 1998, doi: 10.1063/1.872228.

[62] J. Mandrekas, "GTNEUT: A code for the calculation of neutral particle transport in plasmas based on the Transmission and Escape Probability method," *Comput Phys Commun*, vol. 161, no. 1–2, pp. 36–64, Aug.

2004, doi: 10.1016/J.CPC.2004.04.009.

[63] Y. Kim, M. G. Yoo, S. H. Kim, and Y. S. Na, “Development of vector following mesh generator for analysis of two-dimensional tokamak plasma transport,” *Comput Phys Commun*, vol. 186, pp. 31–38, Jan. 2015, doi: 10.1016/J.CPC.2014.09.009.

[64] L. L. Lao *et al.*, “MHD Equilibrium Reconstruction in the DIII-D Tokamak,” *https://doi.org/10.13182/FST48-968*, vol. 48, no. 2, pp. 968–977, 2017, doi: 10.13182/FST48-968.

[65] V. Akcelik, B. Jaramaz, and O. Ghattas, “Nearly Orthogonal Two-Dimensional Grid Generation with Aspect Ratio Control,” *J Comput Phys*, vol. 171, no. 2, pp. 805–821, Aug. 2001, doi: 10.1006/JCPH.2001.6811.

[66] D. Bohm, *The characteristics of electrical discharges in magnetic fields*, Guthrie A. New York: McGraw-Hill, 1949. Accessed: Dec. 31, 2022. [Online]. Available: https://ci.nii.ac.jp/naid/10018428953/

[67] R. Chodura, *Physics of Plasma-Wall Interactions in Controlled Fusion*, Post D.E. New York: Plenum Press, 1986. Accessed: Dec. 31, 2022. [Online]. Available: https://scholar.google.com/scholar_lookup?title=Physics%20of%20Plasma-Wall%20Interactions%20in%20Controlled%20Fusion&publication_year=1986&author=R.%20Chodura

[68] D. Shepard, “A two-dimensional interpolation function for irregularly-spaced data,” *Proceedings of the 1968 23rd ACM National Conference, ACM 1968*, pp. 517–524, Jan. 1968, doi: 10.1145/800186.810616.

[69] T. D. Rognlien, G. D. Porter, and D. D. Ryutov, “Influence of E×B and ▽B drift terms in 2-D edge/SOL transport simulations,” *Journal of Nuclear Materials*, vol. 266–269, pp. 654–659, Mar. 1999, doi: 10.1016/S0022-3115(98)00835-6.

[70] G. v Pereverzev and P. N. Yushmanov, “ASTRA. Automated system for transport analysis in a tokamak,” 2002.

[71] “On the mechanism of RMP-driven pedestal transport and ELM suppression in KSTAR / 김상균 - SNU.” https://snu-primo.hosted.exlibrisgroup.com/primo-explore/fulldisplay?docid=82SNU_INST21801661490002591&context=L&vid=82SNU&lang=ko_KR&search_scope=ALL&adaptor=Local%20Search%20Engine&tab=all&query=any,contains,%EA%B9%80%EC%83%81%EA%B7%A0&facet=rtype,include,dissertations&facet=searchcreationdate,include,2019%7C,%7C2022&offset=0 (accessed Jan. 01, 2023).

[72] A. C. Sontag *et al.*, “SOL effects on the pedestal structure in DIII-D

discharges," *Nuclear Fusion*, vol. 57, no. 7, May 2017, doi: 10.1088/1741-4326/aa6cb6.

[73] P. B. Snyder *et al.*, "A first-principles predictive model of the pedestal height and width: development, testing and ITER optimization with the EPED model," *Nuclear Fusion*, vol. 51, no. 10, p. 103016, 2011.

[74] B. Kim *et al.*, "Investigation of performance enhancement by balanced double-null shaping in KSTAR discharges," *Nuclear Fusion (submitted)*, 2023.

[75] T. Onjun, A. H. Kritz, G. Bateman, and V. Parail, "Magnetohydrodynamic-calibrated edge-localized mode model in simulations of International Thermonuclear Experimental Reactor," *Phys Plasmas*, vol. 12, no. 8, p. 082513, Aug. 2005, doi: 10.1063/1.2007547.

[76] W. Zholobenko *et al.*, "Electric field and turbulence in global Braginskii simulations across the ASDEX Upgrade edge and scrape-off layer," *Plasma Phys Control Fusion*, vol. 63, no. 3, Mar. 2021, doi: 10.1088/1361-6587/abd97e.

[77] D. Galassi *et al.*, "Tokamak edge plasma turbulence interaction with magnetic X-point in 3D global simulations," *Fluids*, vol. 4, no. 1, Mar. 2019, doi: 10.3390/fluids4010050.

[78] T. D. Rognlien, J. L. Milovich, M. E. Rensink, and G. D. Porter, "A fully implicit, time dependent 2-D fluid code for modeling tokamak edge plasmas," *Journal of Nuclear Materials*, vol. 196–198, no. C, pp. 347–351, Dec. 1992, doi: 10.1016/S0022-3115(06)80058-9.

[79] L. Isoardi *et al.*, "Penalization modeling of a limiter in the Tokamak edge plasma," *J Comput Phys*, vol. 229, no. 6, pp. 2220–2235, Mar. 2010, doi: 10.1016/J.JCP.2009.11.031.

[80] S. Wiesen *et al.*, "The new SOLPS-ITER code package," *Journal of Nuclear Materials*, vol. 463, pp. 480–484, Aug. 2015, doi: 10.1016/J.JNUCMAT.2014.10.012.

[81] T. P. E. Modelling *et al.*, "Presentation of the New SOLPS-ITER Code Package for," *Plasma and Fusion Research*, vol. 11, pp. 1–6, 2016, doi: 10.1585/pfr.11.1403102.

Abstract in Korean

친환경적이고 지속가능한 에너지원으로 주목 받아온 핵융합 에너지가 플라즈마를 자기장으로 가두는 토카막 장치에서 그 가능성이 연구되고 있습니다. 한국형 토카막 장치인 KSTAR는 이러한 자기장 구성 중 DN (Double Null)의 장점에 주목하여 SN (Single Null)에서의 전이 실험을 실시하였습니다. 이 실험에서는 전이 과정에서 플라즈마 밀도가 점진적으로 감소함에 따라 성능이 지속적으로 증가함이 관찰되었습니다.

본 연구에서는 해당 KSTAR DN 전이 실험에서 발생한 점진적인 밀도의 저하 현상을 일으키는 세 가지 원인을 제시하고 이를 모델링하여 그 타당성을 보였습니다. 첫번째로 안쪽 디버터 영역에서의 플라즈마 이온의 중성화 및 재이온화를 통한 중심 플라즈마 밀도에 미치는 영향을 자기장 구조를 기준으로 비교하였습니다. 자기장에 평행한 유동만 고려했을 때, 즉 플라즈마 드리프트 현상을 고려하지 않으면 안쪽 디버터에서의 중성화율은 중심 플라즈마 밀도에 대한 영향은 크지 않았습니다. 다음 원인으로는 DN로 전이되면서 ▽B 드리프트의 효과가 변화하여 더 많은 대류를 유도하여 밀도가 저하되는 것입니다. 이는 자기장 구조 차이에 따라 고 자기장 부분에서의 ▽B 드리프트의 대류 방향이 달라져 발생하는 것으로 모델링을 통하여 발견되었습니다. 기존에 드리프트 없이 수렴했던 SN (Single Null)과 DN 플라즈마에 ▽B 드리프트를 추가하여 밀도의 변화를 관찰한 결과 DN 구조에서 밀도가 더 크게 감소하는 것으로 계산되었습니다. 마지막으로 ExB 드리프트로 인한 안쪽 디버터에서 플라즈마 중성화율 증가를 원인으로 제시하였습니다. 자기장의 방향이 그 ▽B 드리프트가 코어 중심부로부터 주 X-point를 향하고 있을 때, ExB의 유동은 그 근처의 바깥쪽 디버터에서 안쪽으로 흐르게 형성됩니다. 하지만 여기서 반대쪽 디버터 근처 영역에서는 그 유동의 방향이 반대가 되어 입자 유동이 바깥쪽 디버터를 향하게 됩니다.

즉, SN 구조에서는 안쪽 디버터에서의 높은 재활용율에 의해 경계 받침 근처 플라즈마 밀도의 큰 상승이 관찰되었지만, DN 구조에서는 반대쪽 유동의 영향으로 그 효과가 매우 작아졌습니다.

더불어 본 연구에서는 해당 플라즈마 모델링을 위해 모델링 요구사항을 정리하고, 이를 충족하는 core-edge-SOL 영역을 통합한 2차원 토카막 플라즈마 수송 모델링 시스템을 구축하였습니다. 중심 플라즈마의 모델링에서는 난류 또는 MHD 모드와 같은 비교적 복잡한 플라즈마 수송 현상을 고려하지 않았습니다. 하지만, 실험적으로 계산된 플라즈마 수송 계수들을 통해 플라즈마 특성을 구현할 수 있었고, SOL과의 2차원적인 상호작용이 포함되어 있기 때문에 중심과 SOL 플라즈마에서 발생하는 현상의 그 반응을 규명하기엔 충분하였습니다. 또한 그리드 생성기의 업그레이드를 통해 토카막 챔버 벽까지의 플라즈마 모델링을 통해 인위적인 경계 조건을 최대한 배제할 수 있었고, 재사용 입자의 수송 현상을 보다 포괄적으로 고려할 수 있게 되었습니다. 따라서 이 시스템은 2차원 드리프트를 구현할 수 있게 됨에 따라 앞서 제안된 이유들을 모델링할 수 있도록 벽에서부터 중심까지의 플라즈마 수송 계산을 수행할 수 있습니다.

주제어: 토카막, 플라즈마, 플라즈마 모델링, 밀도 저하, 플라즈마 드리프트, 자기장 구조
학번: 2017-32731